The Report Committee for Kaimin Yue
Certifies that this is the approved version of the following report:

Study of Brittle/Ductile Layering Effect on Fracture Geometry and Mechanical Behavior by Tri-axial Testing

APPROVED BY
SUPERVISING COMMITTEE:

Supervisor:

Jon E. Olson

John T. Foster

Study of Brittle/Ductile Layering Effect on Fracture Geometry and Mechanical Behavior by Tri-axial Testing

by

Kaimin Yue, B.Nat.Sci.

Report

Presented to the Faculty of the Graduate School of

The University of Texas at Austin

in Partial Fulfillment

of the Requirements

for the Degree of

Master of Science in Engineering

The University of Texas at Austin

May 2015

Dedication

To my parents for their endless love and support

Acknowledgements

I would like to express my sincerest graduate to my supervisor, Dr. Jon E. Olson, for his advice, support, and encouragement throughout my study in the department of Petroleum and Geosystems Engineering. Furthermore, I want to express my appreciation and acknowledge Fracture Research and Application Consortium (FRAC) for providing the financial support for this study. I would also like to thank Dr. John T. Foster for serving on my committee, Dr. Ghislaine De Regge for reviewing my report, Dr. Jon T. Holder for the help in the lab, Dori L. Coy and Frankie Hart for their help in administration and registration, and John Cassibry, Roger Terzian, Daryl Nygaard, and Mark Smith for their technical support.

Special thanks to my colleagues in Dr. Olson's group for their friendship, advice and suggestions. They include Weiwei Wang, Kan Wu, Valerie Gono, Hunjoo Lee, and Nana Asiamah. I also want to thank all my friends for their pleasant company.

Last but not least, I would like to express my deepest graduate to my family for their endless love and support.

Abstract

Study of Brittle/Ductile Layering Effect on Fracture Geometry and Mechanical Behavior by Tri-axial Testing

Kaimin Yue, M.S.E

The University of Texas at Austin, 2015

Supervisor: Jon E. Olson

Hydraulic fracturing has been a widely used technology to produce hydrocarbon from shale plays. A better understanding of the fracturing process is needed to improve oil and gas production. Understanding fracture height growth is one of the main concerns and fracture systems are usually influenced by the presence of layers with contrasting mechanical properties. This study uses a tri-axial test to investigate the fracture geometry and mechanical behavior of brittle/ductile layered samples. Synthetic hydrostone is used as brittle rock, and uncemented sand is used to mimic ductile rock. A series of experiments evaluate the effect of loading speed, confining stress, and layer thickness on the mechanical behavior and fracture geometry of the layered samples. A discrete element method is also used to calculate the mechanical behavior of layered samples and investigate the layering effect.

The tri-axial test results show that the ductile/brittle multilayer becomes more brittle by increasing the number of layers. According to the results, the loading rate has

less effect on thicker layer samples, and the samples are more ductile under higher confining stress. A sensitivity analysis using the discrete element method includes interface properties, number of layers, layer thickness, boundary conditions and edge effects. The results show that the mechanical behavior of brittle/ductile layered samples is highly dependent on the interface properties as well as on the number of layers. The layered samples become stronger and more brittle by increasing interface roughness and friction as well as the number of layers. This work will help better understand brittle ductile behavior of rocks and provide guidelines for the investigation of the brittle ductile layering effect on fracture height containment.

Table of Contents

List of Tables

List of Figures

Chapter 1: Introduction

1.1 Motivation

Hydraulic fracturing is a technology that has been used for decades to improve production from reservoirs (especially low permeability reservoirs). The current technology of hydraulic fracturing enables the production of oil and natural gas from shale, which had not been considered as a reservoir rock from which hydrocarbon is producible. According to Energy Information Administration (EIA), hydraulic fracturing has increased shale gas production in the last decade and is expected to be the most important contributor to natural gas production in the future (Energy Information Administration, Annual Energy Outlook 2012). In 2035, shale gas is expected to account for 49 percent of the total national gas production (Figure 1.1).

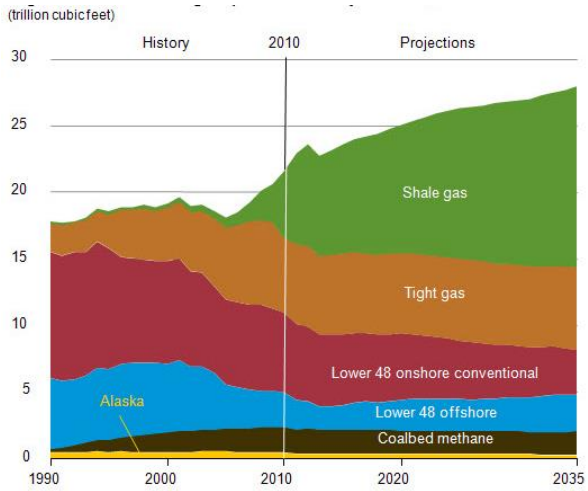

Figure 1.1: Natural gas production by source, 1990-2035 (Energy Information Administration, Annual Energy Outlook 2012)

In order to produce hydrocarbon from shale more efficiently and economically, a better understanding of the fracturing process is needed. Understanding the mechanism of fracture height growth is one of the main concerns (Fisher and Warpinski 2012). Much public discourse questioned whether hydraulic fracturing will contaminate aquifers and pollute groundwater supplies (Osborn et al. 2011).

Micro seismic data and micro deformation data show that hydraulic fractures are contained vertically (Fisher and Warpinski 2012). According to Warpinski, the fracture height is shorter than is predicted by conventional models. The fracture geometry is complex and the fracture height is affected by the layering and heterogeneities of both stress and mechanical properties. A lot of research articles (Fisher and Warpinski 2012; Zhang et al. 2007; Gu et al. 2008) have been published to investigate the mechanism of height containment. In his paper, Warpinski presented the main fracture height containment mechanisms: in-situ stress, elastic modulus contrasts, weak interfaces, layered interfaces, fluid pressure gradients, faults, and high permeability layers.

In our research, we hypothesize a novel fracture height containment mechanism which is caused by the brittle ductile layering effect. As reported in Warpinski's paper (Fisher and Warpinski 2012), seismic data shows that the hydraulic fracture height in Eagle Ford shale is more contained compared to the fracture height in Barnett shale. According to log data, Eagle Ford shale is laminated by alternating carbonate rich (brittle) layers and mud stone rich (ductile) layers and Barnett shale is a calcite rich mud stone, which is quite brittle. The difference between these two shales in both fracture height and characterization motivates us to investigate the brittle ductile layering effect on fracture height containment.

In addition, the outcrops in the Monterey formation of coastal California (Gross et al., 1995) and Kimmeridge Clay Formation (Schopfer et al., 2006; Schopfer et al., 2007a;

Schopfer et al., 2007b) show that the brittle/ductile layered sequence affects the fracture geometry. Observations indicate that mode I (opening) fractures occur in the brittle layers (calcite rich layers), and mode II (shear) fractures appear in the ductile layers (mudstone rich layers). Schopfer et al. (Schopfer et al., 2006; Schopfer et al., 2007a; Schopfer et al., 2007b) investigated the brittle ductile layering effect on the growth of a normal fault using the discrete element method. The results suggest that faults first localize in brittle, strong layers and then link in ductile, weak layers. Their simulation results also reinforce the field observations that fractures in brittle layers are steeply dipping Mode I fractures, and the fractures in ductile layers are shallow dipping faults.

Here I present the brittle ductile layering effect on layered rocks under compaction (which is analogous to the evolution of faults) both experimentally and numerically. Multiple tri-axial experiments with synthetic brittle ductile layered rocks were performed, followed by numerical analysis using the discrete element method. This project aims to evaluate the layering effect on the mechanical response, and the fracture geometry of layered samples under compaction; and to investigate the controlling parameters. Guidelines will be provided for the investigation of the brittle ductile layering effect on fracture height containment.

1.2 OUTLINE

Chapter 1 presents the motivation of the current research. Chapter 2 reviews the literature review related to the current research topic. Chapter 3 provides information on the triaxial experiments. Chapter 4 offers a detailed description of the discrete element method and the simulation models used in PFC3D. Chapter 5 explains the triaxial

experimental and simulation results. Chapter 6 presents the conclusions of the current research and future plans.

Chapter 2: Literature Review

2.1 HYDRAULIC FRACTURING

Hydraulic fracturing is a well stimulation technique in which rock is fractured by high pressure fluid which contains water, sand, and chemicals (Hydraulic fracturing - Wikipedia). Hydraulic fracturing was first applied in the field in 1947 and has become a widely used technology in the last decade. Now hydraulic fracturing is one of the key methods to extract unconventional oil and gas resources. According to George King (2012), over one million fracturing jobs were performed within the U.S. in 2012. Hydraulic fracturing is essential for oil and gas production from shale plays. Due to shale's low permeability, the commercial production of shale gas was impossible before the existence of hydraulic fracturing. According to Energy Information Administration (Annual Energy Outlook 2012), only 1 percent of the United States natural gas production was from shale gas in 2000, but the percentage increased to 20 percent in 2010 (Figure 1.1). By 2035, shale gas is expected to account for 49 percent of the total national gas production.

A hydraulic fracture is created by pumping fracturing fluids at certain rates to increase pressure to exceed the fracture gradient of rock at that location. Fluids injected during a fracturing job can be up to millions of gallons per well (Love 2005). Of all the fracturing fluids, slick water is the most popular. Generally, 99 percent of a slick water fracturing fluid is water and the rest is proppants and chemicals, which are used to reduce friction. The proppants (typically sand or man-made ceramic materials) are designed to keep induced fractures open after injection.

2.2 FRACTURE HEIGHT CONTAINMENT MECHANISM

Understanding the height of hydraulic fractures is one of the main issues in the studies of hydraulic fracturing. In this section, various fracture height containment mechanisms are discussed: in-situ stress, material properties contrast, pressure gradient effect, weak interface, layered interface, and high permeability layers.

2.2.1 In-Situ Stress

The in-situ stress contrast is considered the most important mechanism for fracture height containment (Fisher and Warpinski 2012; Warpinski et al. 1982). The importance of stress on height containment was first studied by Perkins and Kern (Perkins and Kern 1961). The height of a fracture in the reservoir rock is easily restricted if the stress in the upper and lower layers is higher than that of the reservoir rock layer in between. For a symmetric case with three layers (the stress in the upper and lower layer is the same) where the pay zone is surrounded by rocks with higher stress as illustrated in Figure 2.1, the height of a pressurized fracture can be calculated based on linear elastic fracture mechanics. The solution of fracture height in this case was first obtained by Simonson (Simonson et al. 1978), as given by

$$\sigma_2 - P = \frac{2}{\pi}[\sigma_2 - \sigma_1] sin^{-1}\left(\frac{h}{H}\right) - \frac{K_{IC}}{\sqrt{\frac{\pi H}{2}}}, \quad (1)$$

where P is the fluid pressure inside the fracture, $\sigma_1$is the stress in the pay zone, σ_2 is the stress in the upper and lower layer, h is the height of the pay zone, H is the calculated fracture height and K_{IC} is the mode I stress intensity factor, which is widely used in linear elastic fracture mechanics.

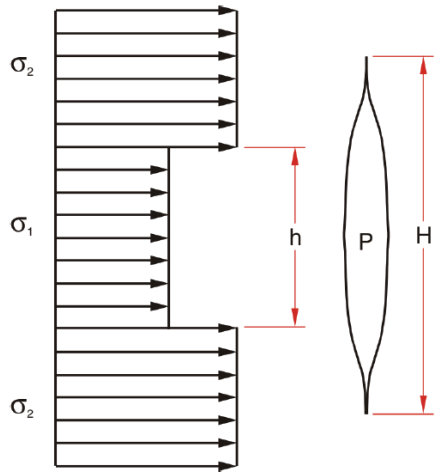

Figure 2.1: Geometry for fracture height calculation. (from Fisher and Warpinski 2012)

According to the solution, fracture height is more restricted in the case of larger σ_2 or K_{IC}. In general, the second term on the right side of equation (1) is small given the fracture toughness values determined from experiments. The in-situ stress mechanism is effective only if there is higher stress in the confining layers.

2.2.2 Material Properties Contrast

Log data shows that reservoirs are laminated with layers of different minerals and these layers have different elastic modulus and fracture toughness (Richard et al. 2011). In this section, the difference in the material properties of layers relates to modulus contrasts and the difference in the fracture toughness of layers.

Simonson et al. (1978) first showed that the difference in modulus between the layers at the interface can effectively blunt the fracture tip. By examining the stress intensity factor at the interface using linear elastic fracture mechanics, Simonson drew the conclusion that the stress intensity factor approaches zero at the interface if the

modulus of the barrier formation is larger than the modulus of the pay zone. In that case, the fracture is blunted and not able to cross from pay zones to barrier zones. However, mineback testing (Warpinski et al. 1982a, b), fracture diagnostic testing (Warpinski et at. 1998), and fracture experiments (Note and Smith, 1981; Teufel and Clark, 1984) showed that Simonson's conclusion is not the case. A more realistic failure criterion rather than the criterion which only considers the stress intensity factor at the fracture tip is needed to model the mechanism of fracture propagation at the interface. As illustrated in Figure 2.2, the mineback results showed that a hydraulic fracture penetrated an interface and propagated from a low modulus zone into a high modulus zone. It is also clear that modulus contrasts can affect fracture width and fluid flow in fractures (Fisher and Warpinski 2012; Eekelen 1982).

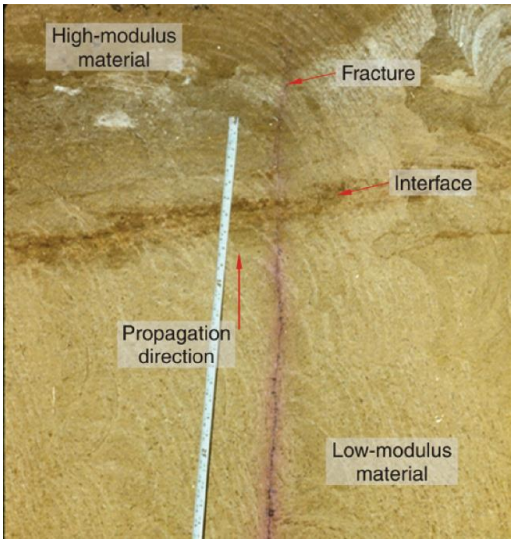

Figure 2.2: Mineback photograph of a fracture propagating from a low modulus zone to a high modulus zone. (from Fisher and Warpinski 2012)

In addition, fracture toughness has an effect on fracture height containment. Larger fracture toughness in confining layers can restrict fracture propagation and induces a high fluid pressure inside a fracture. However, laboratory experiments show that the range of fracture toughness is small for different kinds of rocks, which indicates that the effect of fracture toughness on fracture height containment is negligible (Hsiao and EI Rabaa 1987). However, the scale effect of fracture toughness is not well understood and it is not clear whether fracture toughness has an important effect on large fractures (fractures in hundreds of feet), leaving it as a potential mechanism for fracture height containment (Shlyapobersky et al. 1998).

2.2.3 Pressure Gradient Effects

As a pioneer in investigating fracture height containment, Simonson et al. (1978) also investigated the effect of pressure gradient on fracture height containment. Instead of constant confining stress acting on fractures as illustrated in Figure 2.3, stress varies with depth in a linear gradient. The net pressure is calculated as the difference between the fluid pressure and the confining stress. The figure shows that the fracture has an overpressure at the top. As a result, the downward propagation of the fracture is restricted due to a low net pressure. The important point here is that the pressure gradient effect on fracture height containment is small for short fractures but is not negligible for hydraulic fractures a few hundred feet long.

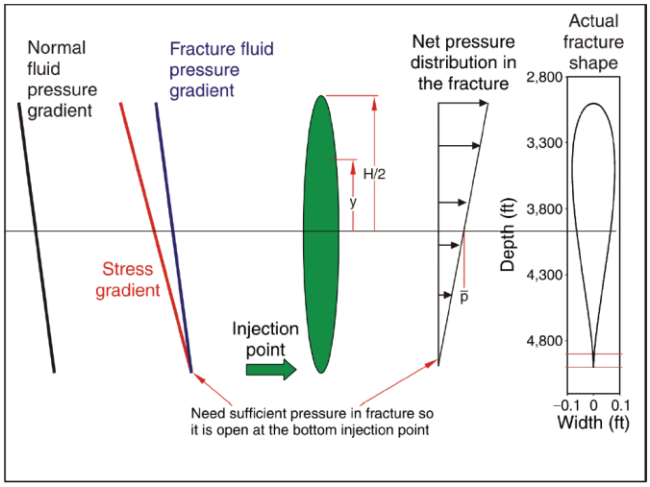

Figure 2.3: Example calculation of fracture size with pressure gradient effects (from Fisher and Warpinski, 2012)

2.2.4 Weak Interface

It is well known that weak interfaces can blunt fracture tips and stop fractures from penetrating interfaces (Fisher and Warpinski, 2012; Zhang et al. 2006; Chuprakov et al. 2013). When a hydraulic fracture reaches a weak bedding plane, the interface is expected to slide due to small friction and cohesion. As a result, the fracture tip is blunted and the fracture is stopped at the interface; otherwise, the fracture will step over at the interface (Cooke and Underwood, 2001). Examples of fracture blunting due to weak interfaces were observed in mine back experiments (Warpinski and Teufel, 1987) and laboratory experiments (Tuefel and Clark, 1984). The important point here is that the weak interface mechanism is believed to be the most important effect of fracture height containment in shallow depth, where friction at the interface is small due to small overburden stress.

2.2.5 Layered Interface

The interaction between natural fractures and hydraulic fractures are investigated with various experimental and numerical methods (Blanton, 1982; Renshaw and Pollard, 1995; Gu and Weng, 2011; Zhang and Jeffrey, 2006; Dahi-Taleghani and Olson, 2011; Wu, 2014; Wang et al. 2013; Lee et at. 2015). The interaction between hydraulic fractures and natural fractures is illustrated in Figure 2.4. Bedding plane interfaces are also considered as geological discontinuities as natural fractures. The mechanisms of the interaction between hydraulic fractures and natural fractures are able to be applied to explain the interaction between hydraulic fractures and bedding planes. A combination of these crossing mechanisms on fracture height containment is presented in Figure 2.5. The containment of hydraulic fracture height is due to restrictions such as kinks, offsets, and termination at the interface. As a result, the geometry of a hydraulic fracture is more complex than a single planar fracture and the fracture height is expected to be contained due to these restrictions.

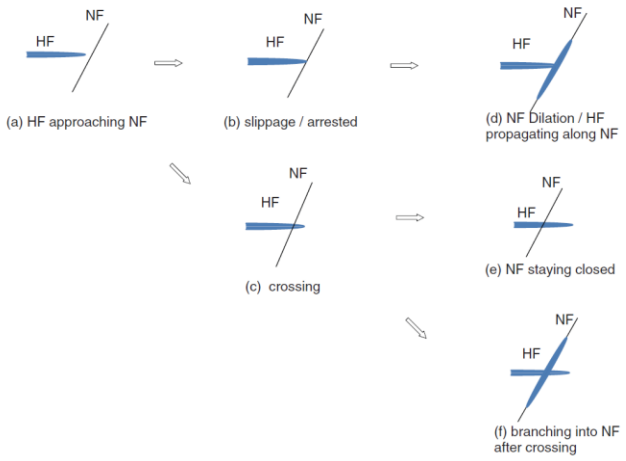

Figure 2.4: Schematic of interaction between hydraulic fractures and natural fractures. (from Gu and Weng, 2011)

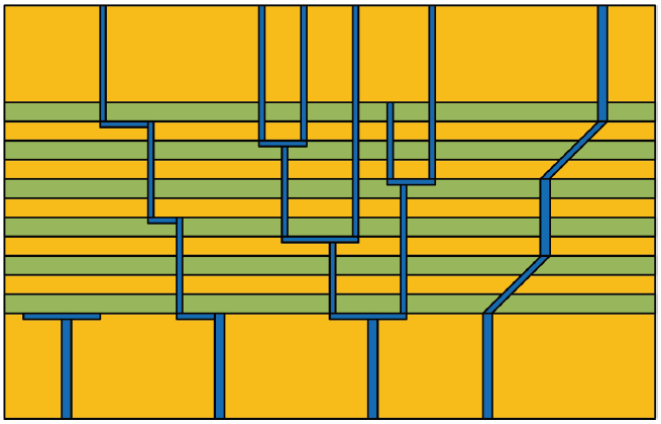

Figure 2.5: Schematic of pathologies for fracture behavior in layered sequence (from Fisher and Warpinski, 2012)

2.2.6 High Permeability Layers

The effect of high permeability layers on fracture height containment is investigated by De Pater and Dong (2009). The experimental results show that injection fluid flowed into high permeability layers and that fractures were contained and did not propagate through the high permeability layers. The numerical results show that the fracture tip tends to close at the high permeability zone and that fracture propagation is possible at higher fluid injection pressure.

2.3 DEFINITION OF BRITTLENESS AND DUCTILITY

Brittleness is an important characteristic to evaluate the fracability of shale (McKeon, 2011). The fracability of shale indicates whether complex fractures can be created in shale plays. Complex fracture networks are preferred in order to increase the production of oil and gas from shale plays. As illustrated in Fig 2.6, more complex

fracture networks can be created when reservoir rocks are more brittle. This section discusses various methods of evaluating rock brittleness: petrophysical based, mineralogy based, and solid mechanics.

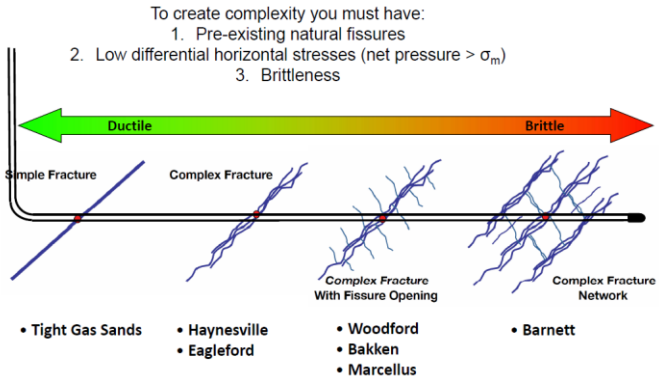

Figure 2.6: Shale fracture characteristics (from McKeon, 2011)

2.3.1 Petrophysical Method

Rickman et al. (2008) presented a definition of rock brittleness based on Poisson's Ratio and Young's Modulus, which are calculated from well log data. The advantage of using a petrophysical interpretation is that it is easier and more common to have well log data available compared to other methods. The rock brittleness is calculated by the following equations

$$YM_{brit} = \frac{100\times(YMS_C-1)}{(8-1)}, \quad (2)$$

$$PR_{brit} = \frac{100\times(PR_C-0.4)}{(0.15-0.4)}, \quad (3)$$

$$BRIT = \frac{(YM_{brit}+PR_{brit})}{2} \quad (4)$$

The definition of static Young's Modulus and Poisson's Ratio is described by Mullen et al. (2007). According to Rickman's definition, a rock is more brittle as the value of Young's Modulus increases and the the value of Poisson's Ratio decreases. . Rickman's quick-look technique might be reasonable because ductile materials will accommodate strain during plastic deformation. The material is more ductile if the Poisson's Ratio is larger. However, According to Reza et al. (2013), both Young's Modulus and Poisson's Ratio are elastic properties and they don't contain any information about post peak potential of the rock. In some cases, rocks with low Young's Modulus and high Poisson's Ratio will experience brittle fractures as well. Figure 2.7 shows a graphical representation of the concept of brittleness. The figure shows that the brittleness percentage of rocks increases towards the lower right corner of the plot, where values of Young's Modulus are larger and values of Poisson's Ratio are smaller.

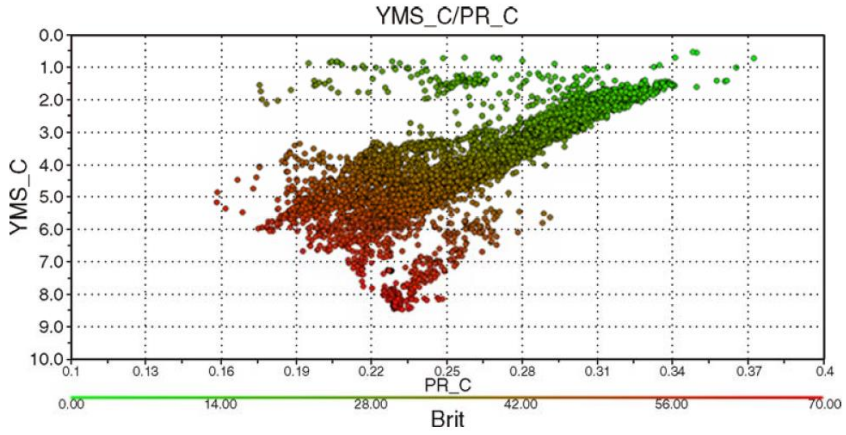

Figure 2.7: A cross plot of Young's Modulus and Poisson's Ratio showing the brittleness percentage increasing towards the lower right corner of the plot. (from Rickman et al. 2008)

2.3.2 Mineralogy Method

Another method to evaluate rock brittleness is based on mineralogy, which is determined from core measurements. To adequately characterize shale, the mineral components are determined from XRD/LIBS analysis. The technique of brittleness determination based on XRD mineralogy is explained by Barree (2002). This technique estimates the value of Young's Modulus and Poisson's Ratio based on the mineral percentage of quartz, carbonate, and clay, which are measured from XRD analysis. The quartz group includes quartz, feldspars, and pyrites. The carbonate group contains calcite, dolomite, and siderite. The clay group includes the total clay. After the calculation of Young's Modulus and Poisson's Ratio based on the mineral percentage, the brittleness of a rock is also determined from the equations mentioned in section 2.3.1. An example of brittleness determination of shale plays based on the mineralogy method is illustrated in Figure 2.8. In general, the rock is more brittle as the percentage of carbonate or quartz increases. However, the rock is more ductile as the percentage of clay increases.

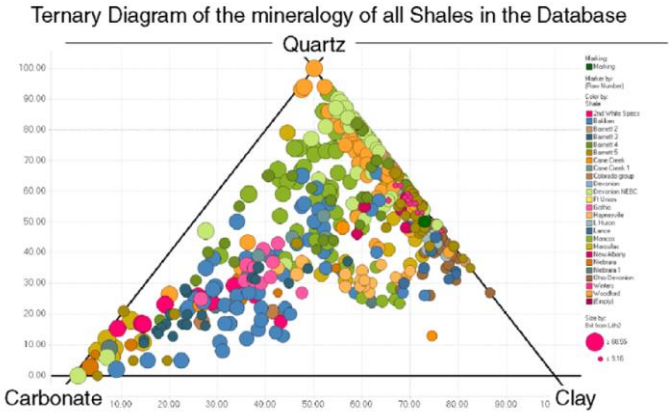

Figure 2.8: Ternary diagram of all shales in the database. The color represents the individual shale and the size of the bubble represents the brittleness determined from the mineralogy method. (from Rickman et al. 2012)

2.3.3 Solid Mechanics Method

The definition of brittleness and ductility based on petrophysical method and mineralogy method is not convincing because Young's Modulus and Poisson's ratio is not related to the post peak behavior. A more appropriate definition of brittleness and ductility is based on the deformation of material. In solid mechanics, ductility is the measurement of the degree of plastic deformation prior to fracture. A material which undergoes very little plastic deformation is brittle. However, a ductile material has the ability to undergo large plastic deformation before breaking. Figure 2.9 illustrates the difference between the deformation of brittle and ductile materials. According to Davis and Reynolds (1996), the mechanical behavior of rocks is dependent on loading rate, temperature, and pressure. Brittle deformation is expected to occur at cool temperature, low pressure, and fast strain rate. However, ductile deformation is expected to occur at high temperature, high pressure, and low strain rate. In the current project of investigation of brittle ductile layering effect, the definition of brittle material and ductile material is based on solid mechanics method. Based on the stress strain curve, hydrostone is a brittle material and a pack of sand will act as a ductile continuum.

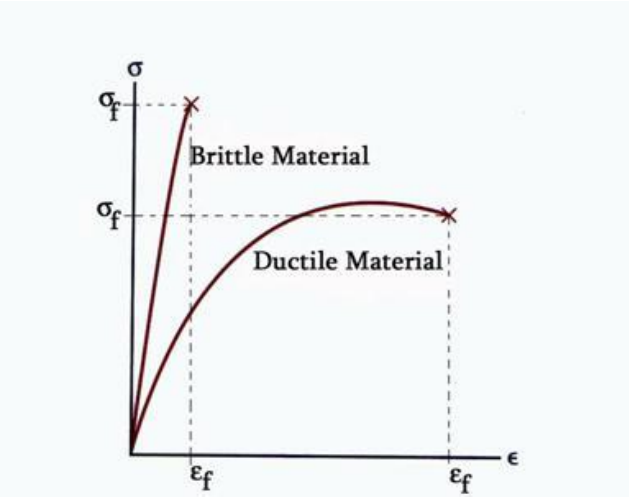

Figure 2.9: The difference in deformation between ductile and brittle materials.

2.4 THE BRITTLE DUCTILE EFFECT ON FAULTS

Due to the difference in mechanical behavior between brittle and ductile rocks, fractures behave differently in brittle layers and in ductile layers. Gross et al. (1995) discovered a normal fault in a brittle ductile layered sequence in Monterey Formation, California. Figure 2.10 shows that in the normal fault, the light color rock in the upper portion is limestone which is brittle and contains a series of Mode-I fractures. However the dark color rock in the lower portion is mudstone, which is ductile and normal faults (Mode-II fractures) are discovered in the ductile layer. Schopfer et al. (2006) found similar fracture systems in a brittle ductile layered sequence in Kimmeridge Bay, UK. As illustrated in Figure 2.11, the formation is laminated with calcareous shale (which is brittle) and mud rich shale (which is ductile). The figure shows lithologically controlled dip changes, with steeper fault dips in brittle layers and shallower fault dips in ductile layers. The modeling results (Schopfer et al. 2006; Schopfer et al. 2007a; Schopfer et al. 2007b) reveal that normal faults in a brittle/ductile layered sequence localize first in

brittle layers as Mode-I fractures, and are later linked to ductile layers as shallow dipping faults.

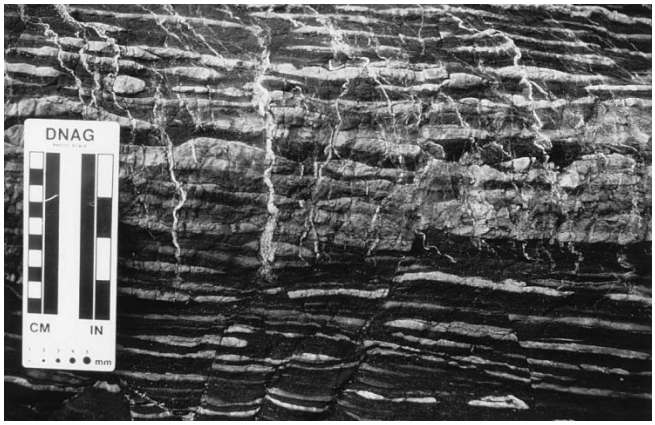

Figure 2.10: A normal fault in the Monterey Formation at Loin's Head, California. The light color rock in the upper half of the graph is limestone, which is brittle and contains a series of Mode-I fractures. The dark color rock in the lower portion is mudstone in which normal faults occur. (from Gross et al. 1995)

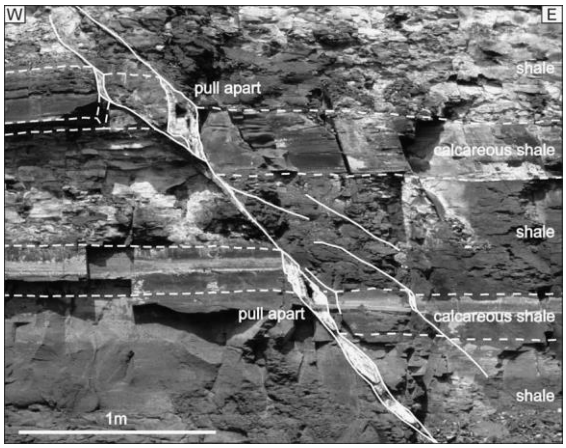

Figure 2.11: A normal fault exposed in a cliff-section east of Kimmeridge Bay, Dorset, UK (from Schopfer, 2006)

2.5 FRACTURE HEIGHT CONTAINMENT IN BRITTLE DUCTILE LAYERS

Based on their observations in the Austin Chalk, Rijken and Cooke (2001) hypothesized that shale has a resistance to fracturing and the thickness of the shale layer may inhibit fracture propagating into the adjacent chalk layer. An analytical crack bridging model (Huang and Zhang, 1995) was used to investigate the thickness dependency on the resistance to fracture propagation. A three layer (chalk-shale-chalk) composite crack bridging model (Figure 2.12) was constructed and the critical shale thickness required to terminate fracture propagation is evaluated to be between 7 and 10 mm for the most frequent thickness of the Chalk layer. However, field observations show that the critical shale layer thickness may be an order of magnitude higher. Furthermore, Rijken and Cooke (2001) also used the FEM model to investigate the influence of shale ductility on fracture termination. The numerical results indicate that fracture propagation is influenced by shale ductility.

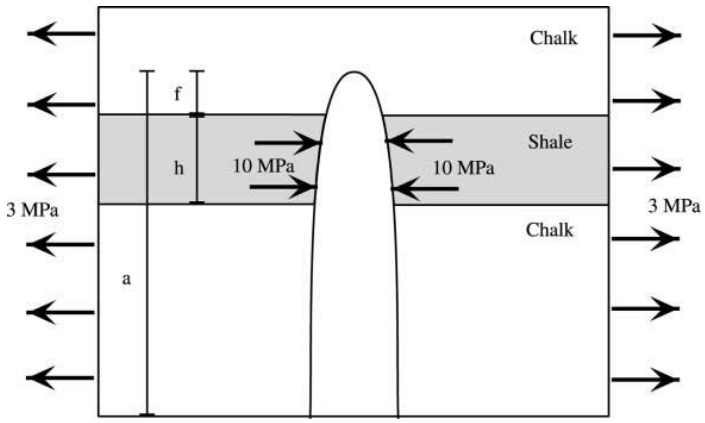

Figure 2.12: Visualization of the three layer crack bridging model (from Rijken and Cooke, 2001)

Friedman et al. (1994) also investigated the effect of the ductile layer on fracture termination. As illustrated in Figure 2.13, the experimental results reveal that clay (which is ductile) can effectively stop a fracture from propagating. The results are clay thickness dependent: fractures penetrate the interface at thin clay layers but fan out and terminate within the clay layer at thick clay layers.

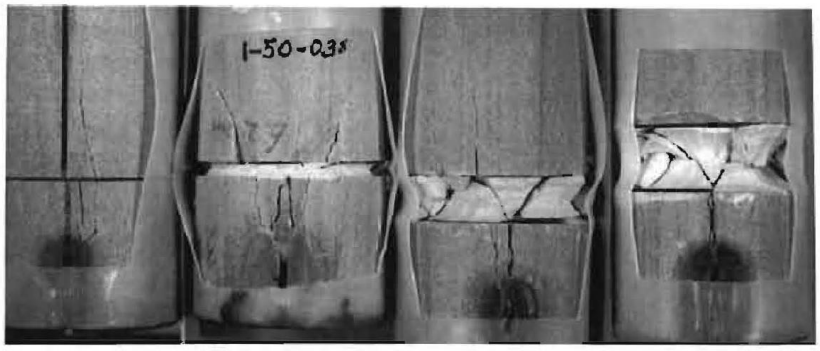

Figure 2.13: Photographs of specimens showing fractures propagating upward from a notch across or into clay layers, whose thickness varies from 0 to 15 mm (from left to right) (from Friedman et al. 1994)

Chapter 3: Experimental Setup

This chapter describes the experimental apparatus used for tri-axial testing. Information on sample preparation and experimental procedures are also presented in detail.

3.1 Experimental Apparatus

The experimental apparatus used in the tri-axial test is shown schematically in Figure 3.1. It contains three parts: a loading device, a pump, and an aluminum confining vessel. The HUMBOLDT loading device provides an axial load, which can be up to 10,000 lbs. The pump is connected to the confining fluid (water) which is contained in the aluminum vessel. As a result, the confining pressure applied on the cylindrical samples is controlled by the pump. The aluminum confining vessel can house a one-inch diameter and two-inch long cylindrical sample. During the tri-axial test, samples are loaded by the HUMBOLDT loading device in axial direction and are also confined laterally by water.

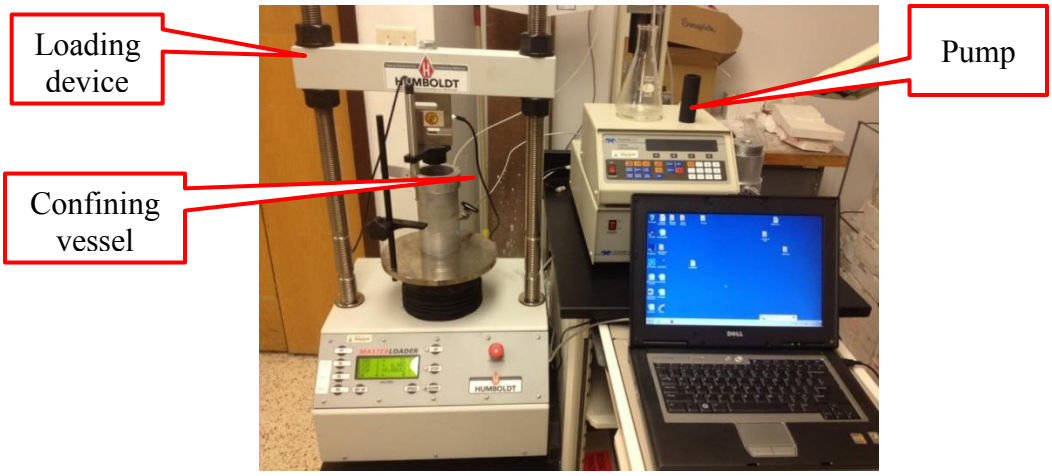

Figure 3.1: Illustration of experimental apparatus

3.2 SAMPLE PREPARATION

The dimensions of the samples used in the tri-axial testing are one inch in diameter and two inches in height. In order to evaluate the mechanical behavior and fracture geometries of the brittle/ductile layered samples, two kinds of samples are used in our experiments. These two samples contain 50 percent brittle material and 50 percent ductile material; however, they have different layer thicknesses. The first sample has two layers with one one-inch brittle layer and one one-inch ductile layer. The second sample has four layers with two half-inch brittle layers and two half-inch ductile layers. Figure 3.2 shows the two types of samples used in testing. In the experiment, hydrostone is used as brittle rock and sand is used to mimic the behavior of ductile rock.

Hydrostone is composed of gypsum and cement, and is produced by United States Gypsum Company (IG-123-F1-50BAG/6-99). Table 3.1 shows the ratio of water and dry cement in weight for hydrostone (Olson et al. 2012; Bahorich 2012). Well mixed liquefied hydrostone is first poured to a one-inch diameter mold and then kept at room temperature for at least three days to make sure it is sufficiently cured.

Material	Dry Cement Weight %	Water Weight %
Hydrostone	75.7	24.3
Gypsum Plaster	63	37

Table 3.1: Mixing percentage for hydrostone and gypsum plaster (from Bahorich, 2012)

The mechanical properties of hydrostone are determined by tri-axial experiments with various confining stresses. Figure 3.3 shows the stress strain curves for hydrostone

with 300 psi, 500psi, 700psi and 1000psi confining stresses. The Mohr-Coulomb criterion can be used to calculate the unconfined compressive stress and the friction coefficient, as given by

$$\sigma_1 = n\sigma_3 + UCS\,, \tag{5}$$

where $\sigma_1$is the peak axial stress, $\sigma_3$is the confining stress, UCS is the unconfined compressive stress, n is the slope of the σ_3 vs. $\sigma_1$curve. n is related to the friction coefficient, as given by

$$n = (f + \sqrt{1 + f^2})^2\,, \tag{6}$$

where f is the friction coefficient. The unconfined compressive stress is measured to be 5846 psi and the friction coefficient is determined to be 0.56. By matching the slope of the linear portion of the stress strain curve, Young's modulus is determined to be around 900,000 psi.

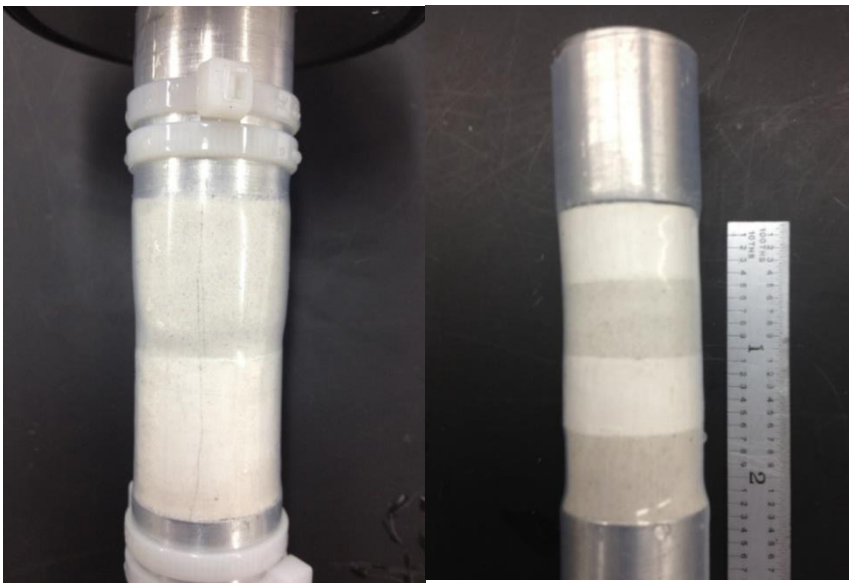

Figure 3.2: Illustration of the two types of samples used

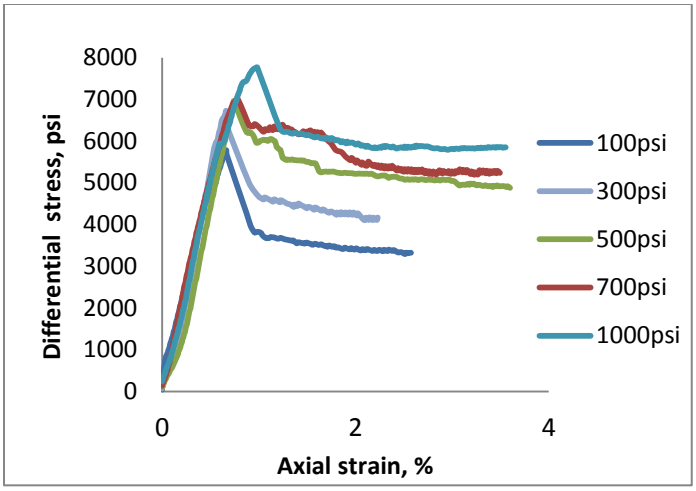

Figure 3.3: The stress strain curves for just hydrostone under various confining stresses. (The strain in this report is engineering strain)

3.3 Experimental Procedures

To investigate the mechanical behavior of the brittle/ductile layered samples, tri-axial testing with various different confining stresses and loading rates was performed. Before the tri-axial tests with layered samples, preliminary tests on just hydrostone or sand are performed to calibrate the micro-properties that are used in numerical models. The next chapter describes the numerical method and calibration procedures.

Chapter 4: Numerical simulation

This chapter describes the discrete element method used to model the movement and interaction of granular particles in tri-axial testing. Information on the model setup and simulation procedures is also presented in detail. Finally, based on the guidelines in the manual (ITASCA, 2008), micro-properties of particles in PFC3D are determined in order to resemble the results of laboratory tests.

4.1 DISCRETE ELEMENT METHOD

Particle Flow Code 3D (PFC3D), which is developed based on the discrete element method (Cundall & Strack, 1979) is used for numerical simulation in this study. It is designed primarily to model the mechanical behavior of an assembly of rigid spherical particles. In PFC3D, brittle rock such as sandstone is modeled by bonding every particle to its neighbors and the resulting assemble is regarded as solid. The variation in the bond type, stiffness and strength, which corresponds to the effect of cement, together with the micro properties of particles enables us to model materials with different macro mechanical properties (Manchanda, 2011; ITASCA, 2008).

The original application of the discrete element method (DEM) was to simulate the behavior of granular material. In contrast to the finite element method, the discrete element method is a numerical model which is capable of simulating the interaction and movement of spherical or circular particles directly instead of applying constitutive laws. The algorithm in DEM includes the application of Newton's second law at each particle and force-displacement law at each contact (ITASCA, 2008). The calculation cycle is a time stepping, explicit scheme and during each time step, contact forces are updated first from the relative motion between two particles at the contact according to force-

displacement law. After that, Newton's second law (Force = mass * acceleration) is used to update the velocity and position of each particle, given the contact forces on each particle. This circulation circle is illustrated in Figure 4.1.

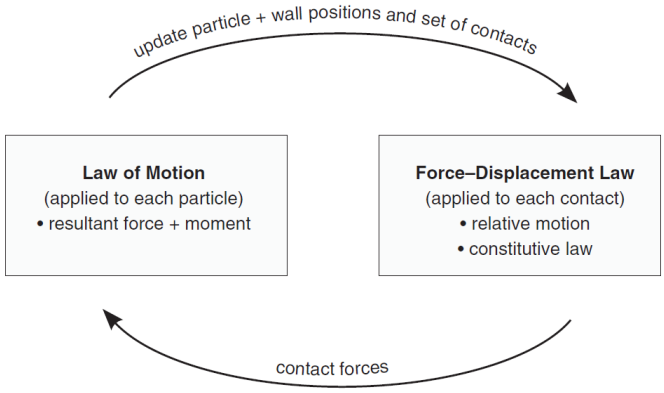

Figure 4.1: The circulation circle in PFC3D (from ITASCA, 2008)

4.2 Contact models

The interactions of particles with other particles and particles with walls occur through the forces and moments at their contact. A contact model describes the physical behavior at the contact. In this chapter, three parts of a contact model will be described: a contact stiffness model, a slip and separation model, and a bonding model (ITASCA, 2008).

4.2.1 Contact Stiffness Models

There are two kinds of stiffness models in PFC3D: the linear contact model and the Hertz-Mindlin contact model. Based on the stiffness models, normal or shear stress at contact can be calculated from the relative normal or shear displacement between two

particles. The normal stiffness is a secant stiff, which relates the normal displacement and normal force. The shear stiffness is a tangent stiff, which relates the increment of shear force and the increment of shear displacement, and can be defined as

$$F_i^n = K^n U_i^n n_i \,, \tag{7}$$

$$\triangle F_i^s = K^s \triangle U_i^s, \tag{8}$$

where K^n is the normal stiffness, K^s is the shear stiffness, F_i^n is the normal force for particle i, F_i^s is the shear force for particle i, $U_i^n$is the normal displacement for particle i, and U_i^s is the shear displacement for particle i. The linear contact model and the Hertz-Mindlin contact model use different ways to calculate contact stiffness. In the linear contact model, the stiffness at the contact is computed analogous to two elastic springs acting in series. As a result, the contact normal stiffness and tangent shear stiffness in the linear contact model can be calculated based on the equations

$$K^n = \frac{k_n^{[A]} k_n^{[B]}}{k_n^{[A]} + k_n^{[B]}}, \tag{9}$$

$$K^s = \frac{k_s^{[A]} k_s^{[B]}}{k_s^{[A]} + k_s^{[B]}}, \tag{10}$$

where subscripts [A] and [B] denote two particles in contact and k is the stiffness.

In contrast to the linear contact model, the Hertz-Mindlin contact model calculates normal stiffness and tangent shear stiffness at contact using a nonlinear method. The expressions for calculating normal contact force and tangent shear stiffness are

$$F_n = \left(\frac{2G\sqrt{2R}}{3(1-v)} \right) u_n^{3/2}, \tag{11}$$

$$k_s = \frac{2(3G^2(1-v)R)^{1/3}}{2-v} F_n^{1/3}, \tag{12}$$

where U^n is the sphere overlap, $\langle G \rangle$ is the shear modulus, $\langle v \rangle$ is the Poisson's ratio, $\bar{R}$ is the average radius of these two particles in contact, F_n is the magnitude of the normal contact force and k_s is the tangent shear stiffness.

4.2.2 Slip and Separation Models

The slip model in PFC3D allows two contacting entities to slip relative to each other. This model enforces no normal strength in tension by checking the overlap between two entities, which is less or equal to zero. In addition, the slip model is always active unless a contact bond (which supersedes the slip behavior and will be described in the following section) is present. The slip model allows slip to occur if the shear tangent force exceeds the maximum allowable shear contact force, which is given by

$$F_{max}^s = \mu |F_i^n|, \tag{13}$$

where F_{max}^s is the maximum allowable shear contact force, μ is the friction coefficient, and F_i^n is the normal force. If $|F_i^s| > F_{max}^s$, slip is allowed to occur and during the next calculation cycle, the updated shear force will be set equal to the maximum allowable shear force.

The separation model allows two contacting entities to separate by checking whether a tension force develops between them and they are no longer bonded.

4.2.1 Bonding Models

Particles are enabled to be bonded together at contact in PFC3D. There are two kinds of bonding models in PFC3D (ITASCA, 2008): the contact bond and the parallel bond. The contact bond can be envisioned as a pair of elastic springs acting over a vanishing area at contact. The parallel bond can be depicted as a set of elastic springs uniformly distributed at a circular cross section area between two particles. This bond reproduces the behavior of finite size cement acting between particles.

The contact bond can produce tensile and shear stress at the contact between two particles. However, the parallel bond is able to provide a connection between two particles that has the ability to resist both forces and moments.

4.3 SIMULATION MODELS

In order to simulate tri-axial testing in PFC3D, models which can represent experimental samples should be generated prior to simulation. This section describes the procedures of sample generation.

4.3.1 Sample preparation procedure

In order to simulate tri-axial testing using PFC3D, models which can represent experimental samples are generated. The main parameters that need to be considered in specimen preparation include sample dimension, porosity, and particle size distribution. The parameters of sample determination are presented in Table 4.1. In the present study, a method of particle generation by radius expansion is employed (ITASCA, 2008). The generated sample in PFC3D is illustrated in Figure 4.2.

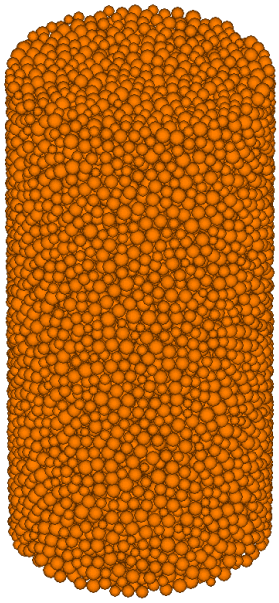

Height, inch	2
Diameter, inch	1
Particle radius, um	500-750
Particle number	15102

Table 4.1: Parameters for model generation

Figure 4.2 Illustration of model

4.3.2 Tri-axial test simulation

In the standard tri-axial test simulation in PFC3D, a cylindrical sample is compressed in axial direction by moving the top and bottom walls towards each other while the curved boundary is assigned a zero displacement boundary condition by applying a rigid wall boundary. After the specimen is prepared, the positions of walls are shifted to reach an equilibrium state at the specific confining stress based on a predefined servomechanism in PFC3D (ITASCA, 2008). During the test, the displacements of top

and bottom walls are monitored in order to calculate the axial strain while the forces exerted on the top and bottom walls are also monitored to calculate the axial stress.

4.3.3 Particle boundaries

In a 'true' tri-axial experiment, a fluid confining pressure condition is applied to the curved boundary of cylindrical samples. In PFC3D, a default wall boundary condition is applied laterally during the axi-symmetric confined compression test simulation; the velocity of walls is controlled by a numerical servomechanism in order to maintain a prescribed confining stress (ITASCA, 2008). However, this wall lateral boundary condition is rigid and not valid compared to the experimental condition because it is not possible for samples to curve. An alternative confining method in PFC3D to create a sheet of particles at the lateral boundary and an assembly of these particles can be considered as a flexible jacket, which is similar to the shrink tube used in experiments. External forces can be applied to each boundary particle and at this point, the whole assembly is under a more realistic confining pressure boundary condition. This approach is described in Manchanda (2012). The challenge associated with this approach is the interaction between the top and bottom walls and particles in the lateral boundary. The axial displacement of walls will affect the axial displacement of particles in the jacket.

The boundary particles are identified by defining a cylindrical ring region which is coaxial with the cylindrical sample. The outer radius of the ring is the radius of the cylindrical sample and the thickness of the cylindrical ring is twice the maximum particle radius. At this point, the particles in this predefined cylindrical ring region are considered boundary particles as shown in Figure 4.3.

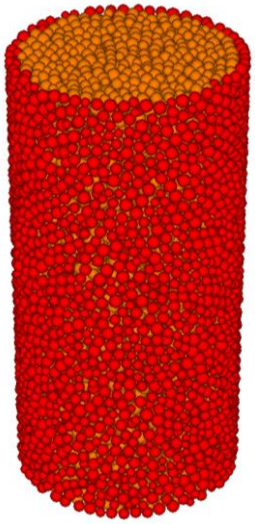

Figure 4.3: Illustration of boundary particles (red particles) in the cylindrical ring

Confining forces applied to the boundary particles are based on the confining stress and particle radius. In order to calculate the applied areas on the identified boundary particles, a sheet of boundary particles is represented by a hypothetic honeycomb with hexagon cells. Figure 4.4 shows a hypothetic honeycomb with hexagon cells which are inscribed by 2D discs. The area of each hexagon cell is considered the applied area of the corresponding inscribed 2D discs. As a result, the applied area of each particle is considered to be $2\sqrt{3}r^2$, where r is the radius of this particle. In order to represent a fluid confining pressure P, the applied force F on each boundary particle can be calculated by (Manchanda 2012)

$$F = \left(P + \sigma_{bp}\right) * 2\sqrt{3}r^2, \tag{14}$$

where $\sigma_{bp}$is the membrane force correction factor, which accounts for the effect of restraining the disintegration of the particle packing by a flexible jacket. Based on the

results provided by British Standards (BS 1377-8 1990), the extra confining stress applied on the boundary particles induced by a flexible jacket is calculated as

$$\sigma_{bp} = \left(\frac{0.038}{D}\right) - 0.0017\varepsilon_z^2 + 0.1295|\varepsilon_z| + 0.0517, \qquad (15)$$

where D is the average diameter of the sample in meters, and ε_z is the axial strain.

After the applied force on each boundary particle is calculated, the value of the x and y components of the applied force can be determined by the equations

$$F_x = -x * \frac{F}{\sqrt{x^2 + y^2}}, \qquad (16)$$

$$F_y = -y * \frac{F}{\sqrt{x^2 + y^2}}, \qquad (17)$$

where x and y are the positions of particles.

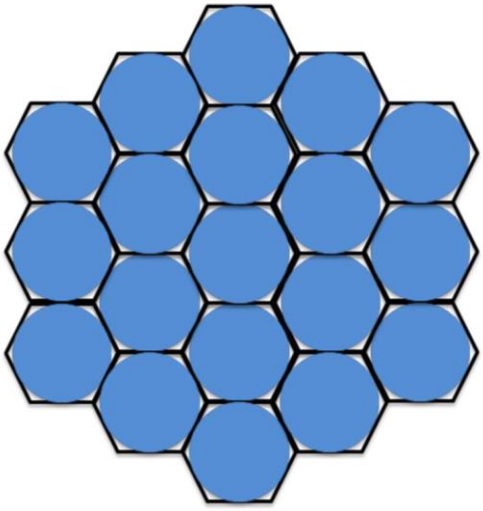

Figure 4.4: Illustration of hypothetic honeycomb with hexagon cells (Manchanda 2011)

4.4 MICRO-PROPERTIES DETERMINATION

Before the simulation using PFC3D, micro-properties of rocks need to be determined. Micro-properties parameters of hydrostone and sand are determined using the methods described in the literature (Manchanda 2011; Park 2006; Potyondy and Cundall 2004). The micro-properties of hydrostone include friction coefficient, normal stiffness (Knn), shear stiffness (Kss), wall stiffness (W_stiff), parallel bond normal stiffness (Pb_knn), parallel bond shear stiffness (Pb_kss), parallel bond normal strength (Pb_nstren), parallel bond shear strength (Pb_sstren), and parallel bond radius multiplier (Pb_radius). The micro-properties of sand include friction coefficient, normal stiffness (Knn), shear stiffness (Kss). Table 4.2 and 4.3 show the micro-properties parameters for hydrostone and sand, respectively.

Grain		Parallel bond	
Knn, N/m	2e7	Pb_kn, N/m^3	6.56e12
Knn/Kss	3.5	Pb_kn/Pb_ks	3.5
W_stiff, N/m	1e6	Pb_rad	0.85
Friction coefficient /particle	0.56	Pb_nstren, N/m^2	4e7
Friction coefficient /wall	0	Pb_sstren, N/m^2	4e7

Table 4.2: Micro-properties parameters for hydrostone

Friction coefficient	1.5
Knn, N/m	1.3e6
Knn/Kss	3.5

Table 4.3: Micro-properties parameters for sand

Based on the micro-properties in Table 4.2 and 4.3, the mechanical behaviors of hydrostone and sand are determined. It is difficult to match various stress strain curves at different confining stresses simultaneously with one set of micro-properties using PFC3D. In this study, the priority is to match the peak stresses, which are used to determine the unconfined compressive stress (UCS) and friction coefficient. The comparison between experimental and numerical results in stress strain curves of hydrostone and sand is illustrated in Figure 4.5. Figure 4.5.a shows that the strength parameters match very well, but the curve shapes don't match well at post peak behavior. In PFC3D, the post peak behavior is related to the particle friction coefficient (Itasca, 2008), loading rate (described in Chapter 5.1), the presence of joints (Park et al. 2004), and etc. Due to these limitations in PFC3D, it is difficult to match the post peak behavior with experimental results. Based on the confining stresses and peak stresses, the unconfined compressive stress and friction coefficient can be calculated. The comparison between experimental and numerical results for hydrostone in UCS, friction coefficient, and Poisson's ratio is shown in Table 4.4. The results show that the values of UCS, friction coefficient and Poisson's ratio determined in PFC3D match very well with the values in experiments.

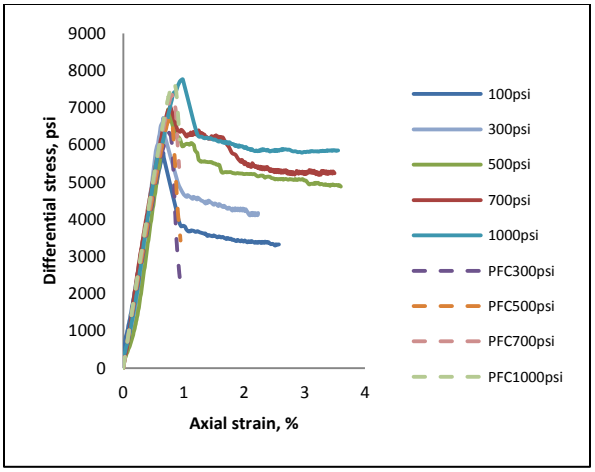

(a)

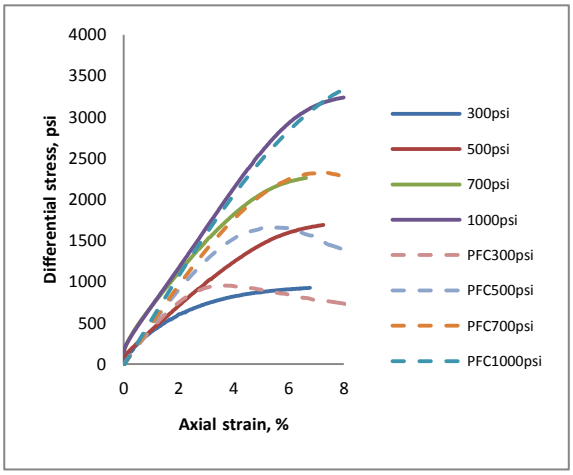

(b)

Figure 4.5: Comparison of stress strain curves of hydrostone (a) and sand (b) between experimental and numerical results

Experiment		PFC	
UCS, psi	5843	UCS, psi	5797
Friction coefficient	0.564	Friction coefficient	0.562
Poisson's ratio	0.28	Poisson's ratio	0.31

Table 4.4: Comparison of UCS, friction coefficient, and Poisson's ratio between experimental and numerical results for hydrostone

Chapter 5: Results and Discussion

In this chapter, both the experimental and numerical results of the brittle ductile layering effect on the fracture geometry and mechanical properties of rocks are presented and discussed. In particular, the effects of loading rate, confining stress, layer thickness, number of layers, interface properties, boundary condition, and edge effect are discussed.

5.1 Effect of loading rate

The material responses of a real material and a DEM model are sensitive to the loading rate. Heard (Heard 1963) performed compression tests with Yule marble at different strain rate conditions and discovered that the higher the strain rate, the stronger the rock will be. In this section, the effect of loading rate on the mechanical behavior of layered samples is examined. Three different loading rates (0.2in/min, 0.02in/min, and 0.002in/min) were used in the tri-axial experiments to evaluate the mechanical behavior of one-inch layer samples and half-inch layer samples (as illustrated in Figure 3.2). Figure 5.1 and Figure 5.2 show the experimental results about stress strain curves at three different loading rates of one-inch layer samples and half-inch layer samples, respectively. The results in Figure 5.1 reveal that the mechanical behavior of one-inch layer samples is ductile under different confining stresses and independent of loading rates. It is possible that one-inch layer samples already reach a quasi-static state at various loading rates in the experiments. However, loading rates have large effects on the mechanical behavior of half-inch layer samples, which behave brittle. The peak stress of half-inch layer samples increases with loading rates and this result is consistent with the mechanical behavior of Yule Marble (Heard 1963).

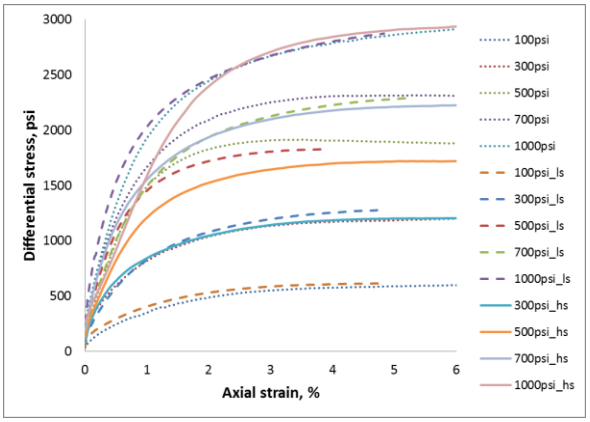

Figure 5.1: Experimental results about stress strain curves of one-inch layer samples at various loading rates (0.2 in/min, 0.02 in/min, and 0.002 in/min) and confining stresses (100 psi, 300psi, 500psi, 700psi, and 1000psi). Hs means a high loading rate which is 0.2 in/min and ls means a low loading rate which is 0.002 in/min.

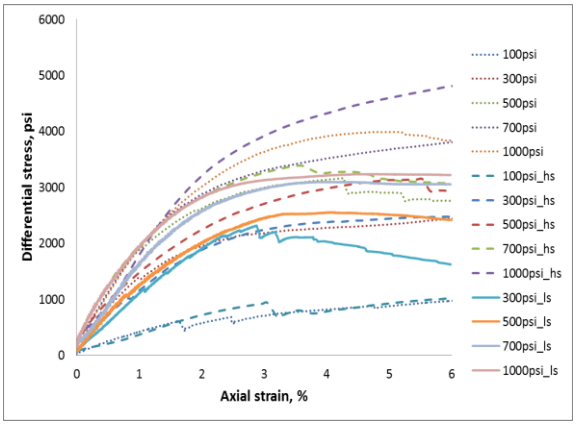

Figure 5.2: Experimental results about stress strain curves of half-inch layer samples at various loading rates (0.2 in/min, 0.02 in/min, and 0.002 in/min) and confining stresses (100 psi, 300psi, 500psi, 700psi, and 1000psi). Hs means a high loading rate which is 0.2 in/min and ls means a low loading rate which is 0.002 in/min.

During the tri-axial simulation in PFC3D, samples are subjected to a loading phase with either a platen based or internal based scheme (ITASCA 2008). In this study, a platen based loading scheme is chosen. In the platen based loading scheme, the specimen is loaded by moving the top and bottom plates towards each other with a specified loading rate which is sufficient to generate a quasi-static solution. In PFC3D, the quasi-static response means the loading rate is slow enough so that there is sufficient time for the system to adjust force redistribution, which accompanies nonlinear events (slip and bond breakage, which is described in Chapter 4.2.2). The top and bottom plates move towards each other at a final velocity v_o, which can be calculated from the expression:

$$v_o = {}^1\!/_2 \, L_o \dot{\varepsilon}_o \tag{17}$$

where L_o is the initial specimen length and $\dot{\varepsilon}_o$ is the strain rate (loading rate). The important point here is that the loading rate used in PFC3D is order of several magnitudes larger than the strain rate used in the experiment. In most cases, small strain rates are not used in discrete element method simulation due to computation cost. The strain rate used in this study is 0.1 s^{-1}, corresponding to a loading velocity of 6 in/min. Tri-axial numerical experiments with different strain rates were tested to verify that the results are acceptable with 0.1 s^{-1} strain rate. Figure 5.3 compares the stress strain curves of hydrostone at 300 confining pressure with two different loading rates: 0.1 s^{-1} and 0.001 s^{-1}. A strain rate of 0.001 s^{-1} corresponds to the top and bottom plates moving at a velocity of 0.06 in/min. The results reveal that the two curves have the same linear section and almost the same peak stress. The only difference might come from the post peak section. The stress drops more quickly after peak at the strain rate of 0.001 s^{-1} compared to the stress change after peak at the strain rate of $0.1s^{-1}$. It is possible that the 0.1 s^{-1} strain rate is too fast and there is not sufficient time for force redistribution during

bond breakage after samples fail. However, the post peak behavior is not used to calculate material properties in this study. Furthermore, samples are brittle according to the post peak failure at two loading rates. The 0.1 s^{-1} strain rate is chosen because of the much cheaper computation cost and reasonable results.

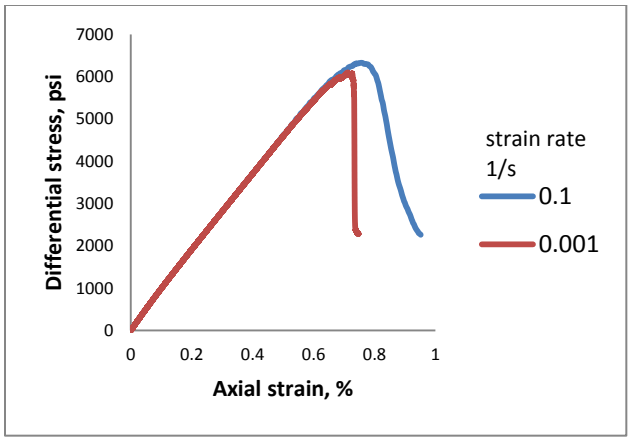

Figure 5.3: Stress strain curves of hydrostone at 300 confining pressure with two loading rates: 0.1 s^{-1} and 0.001 s^{-1}.

5.2 EFFECT OF CONFINING STRESS

The mechanical response of rocks in tri-axial experiments or in DEM simulation is also dependent on confining stress. Donath (1970) investigated the mechanical behavior of limestone deformed at a variety of confining pressures. The results show that both strength and plasticity increase with greater confining pressures, which is quite consistent with the results in this study. According to the stress strain curves at different confining pressures illustrated in Figure 5.1 and Figure 5.2, for the same loading velocity, peak stress increases with confining stress. The results also reveal that there is zigzag at low confining stress, which is due to brittle failure (Figure 5.2). However, the stress strain

curve at high confining stress is quite smooth. The difference in post peak failure at different confining stress reveals that rocks become more ductile at higher confining stress. In summary, both strength and ductility of rocks increase with confining pressures.

5.3 EFFECT OF LAYER THICKNESS

According to the post peak behavior illustrated in Figure 5.1 and Figure 5.2, half-inch layer samples are more brittle and stronger compared to one-inch layer samples. A number of reasons might explain this behavior: layer thickness, number of layers, interface properties, and so on. The mechanical properties of hydrostone or sand might depend on the thickness of samples. For example, hydrostone with different thicknesses may have different mechanical properties, which are able to affect the mechanical behavior of layered samples. In this section, the effect of layer thickness is examined by the DEM simulation with PFC3D. Tri-axial tests of homogeneous samples with different thicknesses (0.25 inch, 0.5 inch, 1 inch, 2 inches, and 4 inches) are performed. Figure 5.4.a shows the stress strain curve of hydrostone with different sample thicknesses at 300 psi confining pressure and Figure 5.5.a shows the peak stress of hydrostone samples with different layer thicknesses. According to Figure 5.4.a, the stress strain curves hardly change for hydrostone samples with thicknesses from 1 inch to 4 inches. The results also indicate that the peak stress increases with sample thicknesses from 0.25 inch to 1 inch and hardly changes with sample thickness from 1 inch to 4 inches. Figure 5.4.b shows the stress strain curve of sand with different sample thicknesses at 300 psi confining pressure. Figure 5.5.b shows the peak stress of sand samples with different thicknesses. The results show that the peak stress and stress strain curve are almost the same for sand samples with different thicknesses.

In summary, the results show that the peak stress of one-inch hydrostone samples is higher than that of half-inch hydrostone samples. Moreover, the peak stresses of one-inch thick sand samples and half-inch thick sand samples are almost the same. If the layer thickness effect on the strength of hydrostone and sand is considered, the peak stress of one-inch layer samples should be larger than the peak stress of half-inch layer samples. However, according to the stress strain curves of layered samples (Figure 5.1 and Figure 5.2), the peak stress (around 2200 psi) of half-inch layer samples is much larger than the peak stress (around 1000 psi) of one-inch layer samples at the same confining. As a result, the mechanical response difference between one-inch layer samples and half-inch layer samples is not due to the change in layer thickness.

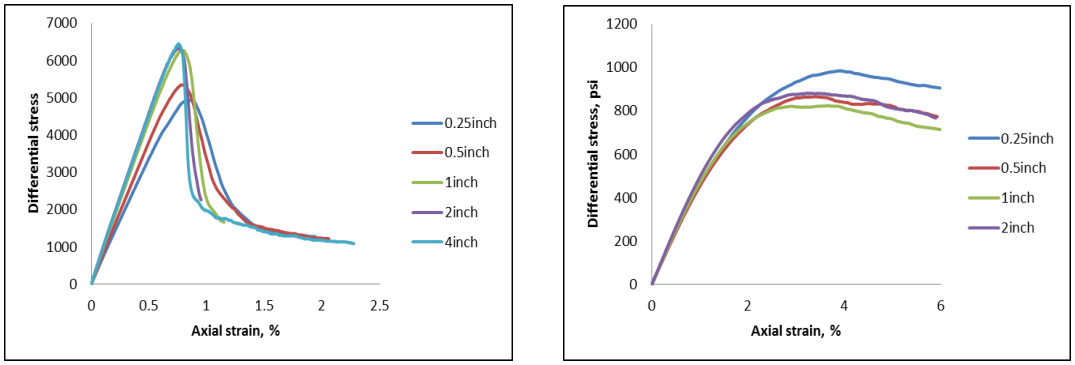

(a) (b)

Figure 5.4: Stress strain curves of hydrostone (a) and sand (b) with different thicknesses at 300 psi confining

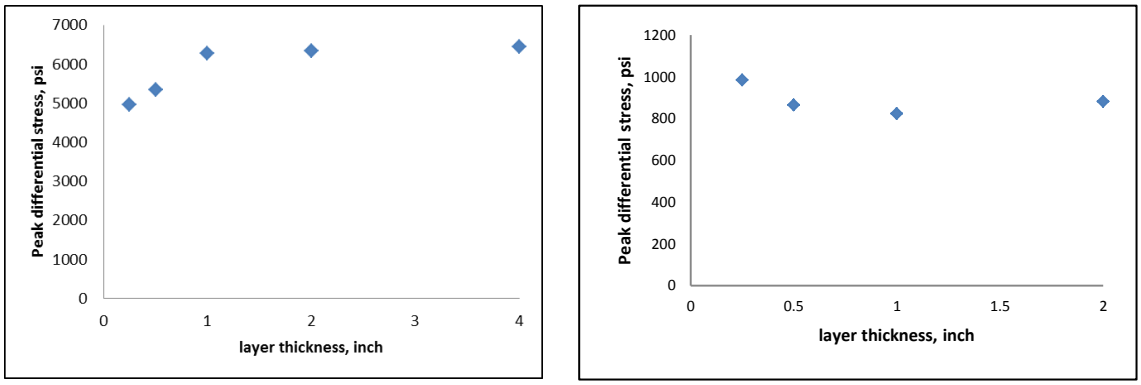

(a) (b)

Figure 5.5: Peak stress of hydrostone (a) and sand (b) with different thicknesses at 300 psi confining

5.4 EFFECT OF NUMBER OF LAYERS

This section examines the effect of number of layers on the mechanical response of layered samples. Four samples with different number of layers were used in the tri-axial tests with PFC3D (Figure 5.6). The red particles are sand and the brown particles are hydrostone. Figure 5.7.a shows the stress strain curves for layered samples with different number of layers. Figure 5.7.b shows the peak stress of samples with different number of layers. It can be observed that peak stress increases with the number of layers. The results reveal that layered samples are strengthened by increasing the number of layers. By increasing the number of layers, the number of interfaces in samples also increases and there is a larger resistance to prevent samples from expansion due to the friction at the interface. This mechanism is also mentioned in Bourne (2003). He investigated the effect of the contrast in elastic properties between rock layers on the initiation and orientation of tensile failure under uniform remote compression. As illustrated in Figure 5.8, friction at the interface occurs due to different lateral strains

caused by the difference in material properties between soft and stiff layers. As a result, layered samples become stronger by increasing the number of layers.

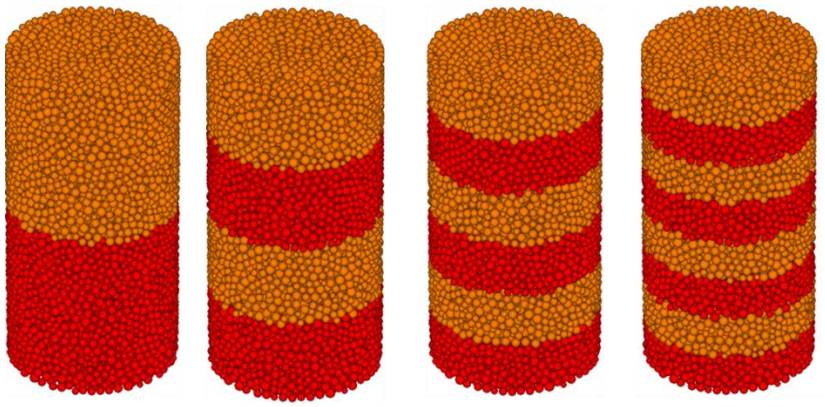

Figure 5.6: Four samples with different number of layers investigate the effect of number of layers using PFC3D (red particles represent sand and brown particles represent hydrostone).

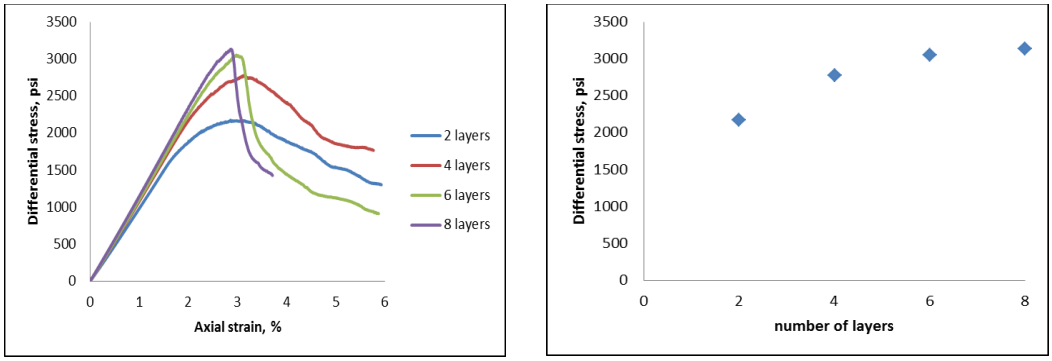

(a) (b)

Figure 5.7: (a) Stress strain curves of layered samples with different number of layers at 300 psi confining; (b) Peak stress of layered samples with different number of layers at 300 psi confining

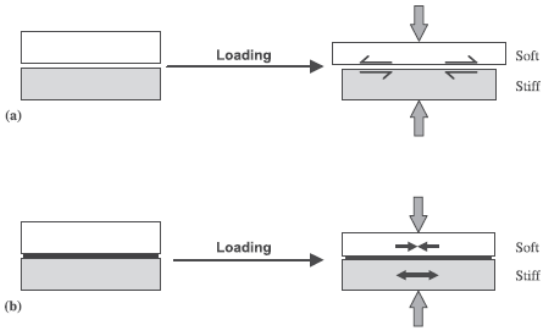

Figure 5.8: The role of bonding in a mechanically layered system. (a) The nonbonded case: Free slip occurs along the interface. (b) The bonded case: No slip occurs along the interface and parallel stresses in soft and stiff layers are different. (from Bourne, 2003)

The above results show that samples are strengthened by increasing the number of layers for a fixed dimension. To evaluate the effect of number of layers on the mechanical properties of layered samples, cases with different sample heights by adding the number of layers are also investigated. Figure 5.9 shows three samples with different heights. The stress strain curves and peak differential stress of samples with different heights are illustrated in Figure 5.10a and Figure 5.10b, respectively. The results show that the peak differential stress and the linear portion of stress strain curves are almost the same for samples with different heights (2 inches, 3 inches, and 4 inches). In order to explain this behavior, the height of fractures in samples needs to be taken into account. Because the diameter of samples is fixed at 1 inch, the height of fractures in samples is about 2 inches if the friction coefficient is assumed to be 0.6. The height of shear failure surfaces in samples (Figure 5.11) is probably the same for samples with different heights. By including the failure behavior of samples, the strength of samples more likely depends

on the height of fractures rather than on the height of samples when the height of samples is larger than that of fractures.

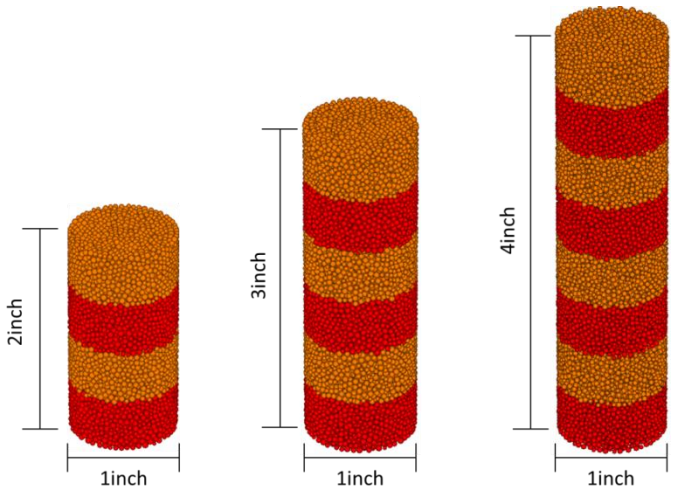

Figure 5.9: Three samples with different heights (red particles represent sand and brown particles represent hydrostone).

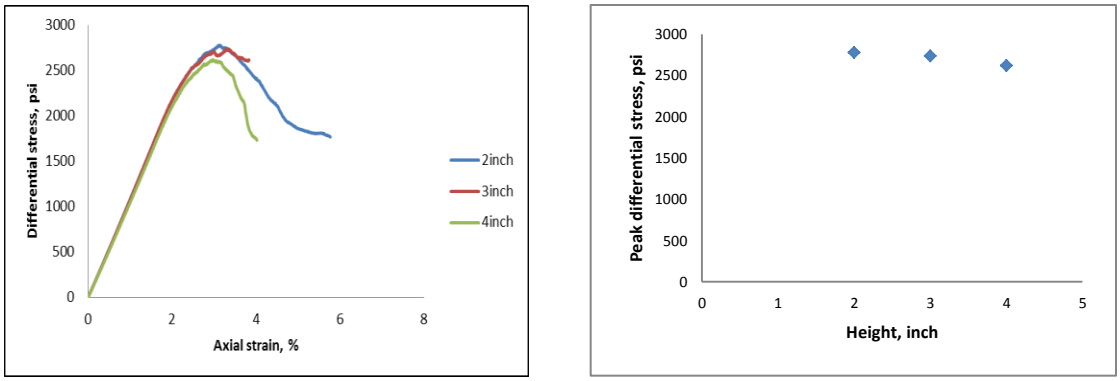

(a) (b)

Figure 5.10: (a) Stress strain curves of layered samples with different heights at 300 psi confining; (b) Peak stress of layered samples with different heights at 300 psi confining

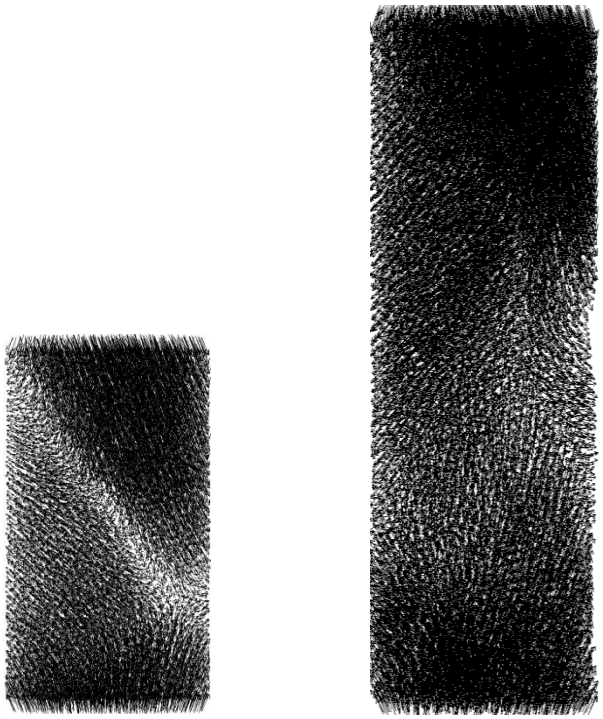

(a) (b)

Figure 5.11: Shear failure surface height indicated by the displacement profile of particles after failure for samples with different heights: 2 inches (a) and 4 inches (b).

5.5 EFFECT OF INTERFACE PROPERTIES

The results in the previous section show that the number of layers (the number of interfaces) within the fracture height plays a significant role in the mechanical response of layered samples. The present section discusses the effect of interface properties on the mechanical response of layered samples. The interface between brittle materials and ductile materials is considered to be frictional without any cohesion. The effect of interface properties includes the friction coefficients assigned to the particles at the interface and the roughness at the interface (Figure 5.11).

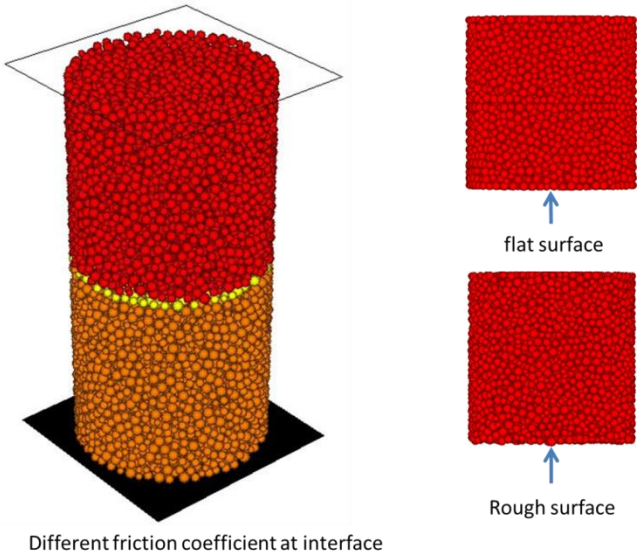

Figure 5.12: (a) Interface particles in yellow (b) Interface surfaces with different roughness

5.5.1 Friction Coefficient at the Interface

This section investigates the effect of friction coefficients at the interface (Figure 5.11.a) on the mechanical properties of layered samples. In the simulation, different friction coefficients are assigned to the particles at the interface. In order to eliminate the roughness effect of the interface, smooth surfaces at the interface are used. Figure 5.12 shows the stress strain curves for samples with different friction coefficients at smooth interfaces. The X axis shows the axial strain and the Y axis shows the differential stress. The results show that stress increases if the friction coefficient increases, and that samples are stronger if the friction coefficients of the interface particles increase. Friction forces at the interface increase with the friction coefficients and as a result, samples are stronger due to larger friction forces.

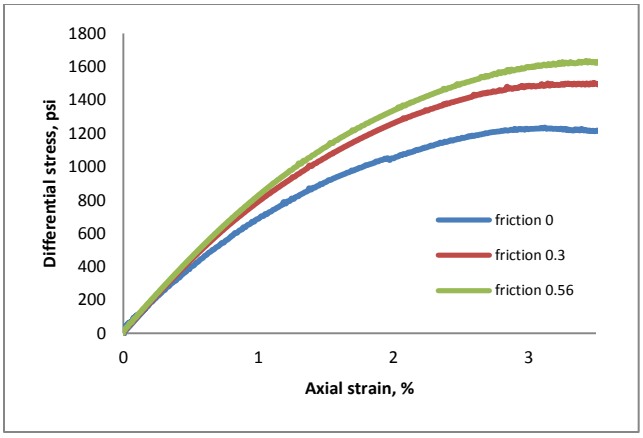

Figure 5.13: Stress strain curves of layered samples with different friction coefficients at the interface

5.5.2 Roughness at the Interface

The roughness at the interface can also have a significant effect on the mechanical properties of layered samples. In order to evaluate the roughness effect of interfaces, two kinds of interface surfaces (smooth surfaces and rough surfaces illustrated in Figure 5.11.b) are used in the simulation. In the simulation, the confining pressure is 300 psi and the friction coefficient of the interface particles is 0.56. The stress strain curves are illustrated in Figure 5.13. The blue curve shows the results for smooth surfaces and the red curve shows the results for rough surfaces. The results indicate that rough surfaces will make the sample stronger compared to the smooth surface. This behavior might be due to the fact that rough interfaces provide a stronger resistance to prevent samples from expanding.

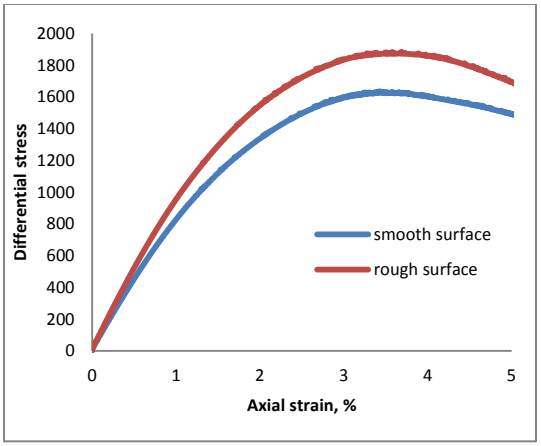

Figure 5.14: Stress strain curves of layered samples with different roughness at the interface

5.6 EFFECT OF BOUNDARIES

In the tri-axial experiments, cylindrical samples are laterally surrounded by water, which applies confining pressure. Water in the vessel is connected to a pump and the fluid pressure of the water is controlled by the pump. As a result, the lateral boundary condition of the samples in the tri-axial experiments is a stress boundary condition. However, a displacement boundary condition is a reasonable condition for rocks in the underground. The stress boundary condition means that the same stress is applied to different layers and that the displacements in layers are different due to different material properties; however, displacement boundary condition means that the same displacement is applied to different layers and as a result, stresses in different layers are different. In this section, the effect of different boundary conditions (stress boundary condition and displacement boundary condition) on the mechanical properties of layered samples is investigated using the discrete element method. In PFC3D, if a particle assembly is compacted within a set of confining walls, these walls can act as displacement boundary

constraints (ITASCA 2008). The information on stress boundary condition in PFC3D is described in Chapter 4.3.3.

Figure 5.14 shows the displacement profile of particles after sample failure for one-inch layer samples. The top layer is hydrostone and the bottom layer is sand. The left sample shows the case of the stress boundary condition and the right sample shows the case of the displacement boundary condition. As illustrated, in the case of displacement boundary condition, particles in the lateral boundary have the same lateral displacement. However, in the case of stress boundary condition, sand expands more laterally than hydrostone because hydrostone is stiffer than sand.

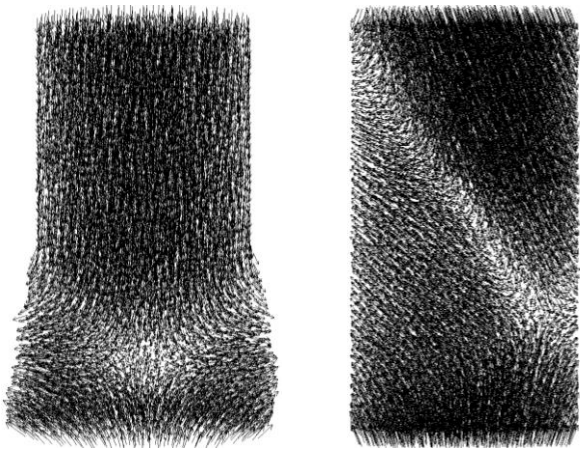

(a) (b)

Figure 5.15: Displacement profile of particles after sample failure for one-inch layer samples with stress boundary condition (a) and displacement boundary condition (b).

5.7 EFFECT OF EDGE

This section examines the edge effect on the mechanical response of layered samples. In the experiments, the top and bottom of samples are connected with cylindrical rams (Figure 3.2). The rams are composed of aluminum, which is much stiffer than the materials (hydrostone and sand) used in the experiments. Moreover, hydrostone is much stiffer than sand. The mechanical properties of layered samples might depend on whether hydrostone or sand is connected to the aluminum cylindrical rams. In order to examine this edge effect, two types of samples are created in PFC3D (Figure 5.15.a). In the figure, hydrostone is in red and sand is in brown. The top and bottom of the left sample is hydrostone, which is connected to the rigid plates in simulation. In contrast, the top and bottom of the right sample is sand. Figure 5.15.b shows the stress strain curves of these two samples. The X axis shows the axial strain and the Y axis shows the differential stress. The blue curve shows the result of the left sample and the blue curve shows the result of the right sample. According to the results, the stress strain curves of these two samples are almost the same, which indicates that the edge effect on the layered samples is negligible. In addition, another group of samples with more layers (Figure 5.16.a) is used to reinvestigate the edge effect. Figure 5.16.b shows the stress strain curves of these two samples and those results also indicate that the effect of edge on the mechanical response of layered samples is negligible.

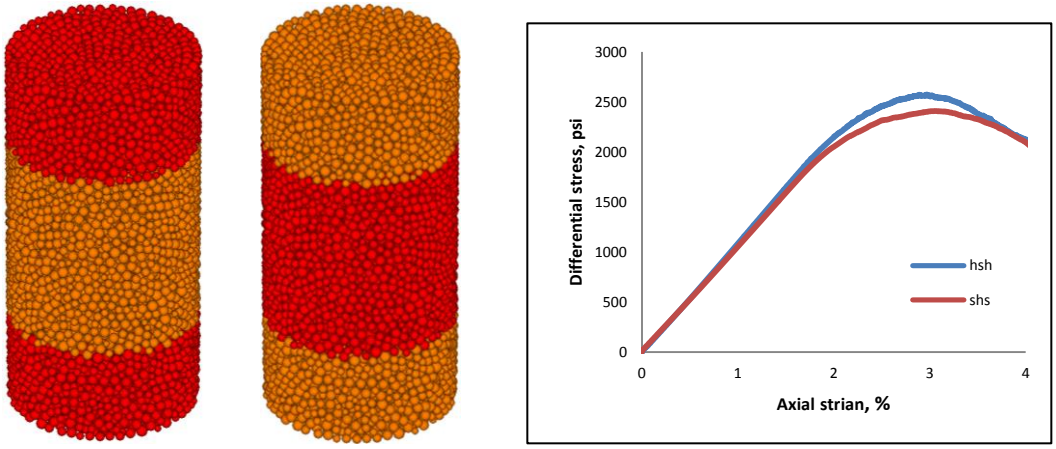

(a) (b)

Figure 5.16: (a) Two types of samples, hydrostone in red and sand in brown (b) Stress strain curves of layered samples with different edges (h means hydrstone and s means sand)

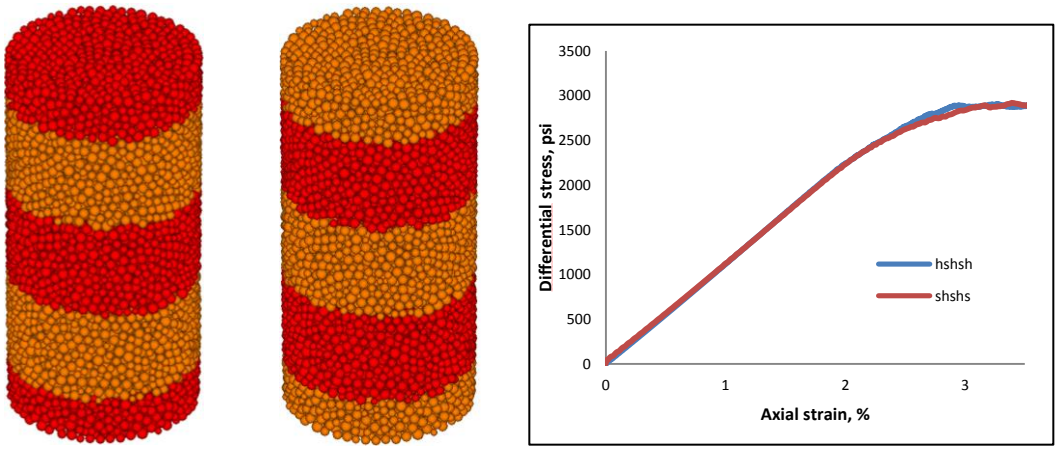

(a) (b)

Figure 5.17: (a) Two types of samples, hydrostone in red and sand in brown (b) Stress strain curves of layered samples with different edges (h means hydrstone and s means sand)

Chapter 6: Conclusions and Future Plans

In this report, tri-axial experiments with synthetic samples are used to investigate the brittle ductile layering effect on the mechanical properties and fracture geometries of layered samples. In addition, various models with the discrete element method are used to examine the effect of loading rate, confining stress, layer thickness, number of layers, interface properties, boundary condition, and edge.

The experimental results show that both one-inch layer samples and half-inch layer samples are more ductile and stronger under higher confining pressures and that the loading rate has less effect on the mechanical properties of samples with thicker layer thickness. The important point here is that the brittleness of samples is dependent on the number of layers and as a result, half-inch layer samples are more brittle and stronger than one-inch layer samples.

The sensitivity analysis using the discrete element methods reveals that the number of layers and the interface properties are the two main parameters to control the layering effect. Samples are stronger and more brittle when the number of layers or the friction at the interface is increasing. This layering effect might be due to the friction at the interface which acts as a resistance to prevent samples from expanding.

The implication of this study is to provide insight into the brittle ductile behavior of rocks and provide guidelines for the investigation of the brittle ductile layering effect on fracture height containment.

Future plans involve investigating the brittle ductile layering effect on fracture height containment using wedge experiments, which are quite similar to the methods in Friedman's paper (Friedman et al. 1994). The effect of layer thickness, interface properties and fracture initiation location (whether fractures are initiated in ductile layers

or brittle layers) will be examined. Furthermore, models coupled with fluid will be developed to investigate the layering effect on fracture height containment using the discrete element method or the finite element method.

Reference

Adam H. Love. 2005. Fracking: The Controversy over Its Safety for the Environment. Johnson Wright, Inc. Retrieved 2012-06-10.

Bahorich, B.L. 2012. Examining the Effect of Cemented Natural Fractures on Hydraulic Fracture Propagation in Hydrostone Block Experiments, Master thesis.

Barree, R. 2002. Introduction to Gohfer and Stimulation Design, Internal publication. Barree and Associates.

Borstmayer R., Stegent N., 2011. Wagner A. et al. Approach Optimizes Completion Design. The American Oil and Gas Reporter. August 2011.

Bourne, S.J. 2003. Contrast of elastic properties between rock layers as a mechanism for the initiation and orientation of tensile failure under remote compression. Journal of Geophysical Research, 108 (2003), p. 2395

BS 1377-8, 1990. Methods of test for soils for civil engineering purposes. Shear strength tests (effective stress). British Standard, P.36.

Chuprakov D, Melchaeva O, Prioul R (2013) Hydraulic fracture propagation across a weak discontinuity controlled by fluid injection. In: Bunger A, McLennan J, Jeffrey R (eds) Effective and sustainable hydraulic fracturing, InTech, pp 183–210.doi:44712

Cooke, ML., Underwood, CA. 2001. Fracture termination and step-over at bedding interfaces due to frictional slip and interface opening. J Struct Geol. Feb-Mar; 23(2-3): 223-38.

Cundall, P.A., Strack, O.D.L. 1979. A discrete numerical model for granular assemblies, Geotechnique, 29 (1) (1979), pp. 47–65

Dahi-Taleghani, A, and J.E. Olson. 2011. Numerical modeling of multistranded-hydraulic-fracture propagation: accounting for the interaction between induced and natural fractures. SPE Journal. September, 575-581.

De Pater, C. J., and Y. Dong, 2009, Fracture containment in soft sands by permeability or strength contrasts: SPE Hydraulic Fracturing Technology Conference, The Woodlands, Texas, January 19–21, 2009, SPE 119634, 9 p.

Donath, F. A., 1970, Some information squeezed out of rock, Am. Scientist 58, 54–72

Energy Information Administration, Annual Energy Outlook 2012, http://www.eia.gov/forecasts/aeo/source_natural_gas_all.cfm#growth

Fisher , K. , and N. Warpinski . 2011 . Hydraulic fracture-height growth: real data. Paper SPE 145949 presented at the Annual Technical Conference and Exhibition, Denver, Colorado. DOI: 10.2118/145949-MS

Friedman, M., O. Kwon, and V. L. French, 1994, Containment of natural fractures in brittle beds of the Austin chalk, rock mechanics, models and measurements challenges from industry, in P. P. Nelson and S. E. Laubach, eds., Proceedings of the 1st North American Mechanics Symposium: Texas, Balkema, p. 833–840.

Gross, M.R., Fischer, M.P., Engelder, T., Greenfield, R.J., 1995. Factors controlling joint spacing in interbedded sedimentary rocks: Integrating numerical models with field observations from the Monterey Formation, USA. In: Ameen, M.S. (Ed.), Fractography: Fracture Topography as a Tool in Fracture Mechanics and Stress Analysis. Geol. Soc. London Spec. Publ. 92, 215–233.

Gu, H., Weng, X., Lund, J., Mack, M., Ganguly, U. and Suarez-Rivera, R. 2011. Hydraulic fracture crossing natural fracture at non-orthogonal angles: A criterion, its validation and applications. SPE 139984, SPE Hydraulic Fracturing Conference and Exhibition, The Woodlands, Texas, January 24-26.

Heard, H.C. 1963. Effect of large changes in strain rate in the experimental deformation of Yule Marble. J. Geol. 71, 162-195.

Huang, Y., Zhang, H.W., 1995. The role of metal plasticity and interfacial strength in the cracking of metal/ceramic laminates. Acta. Metall. Mater. 43 (4), 1523-1530.

Hsiao, C. and El Rabaa, A.W. 1987. Fracture Toughness Testing of Rock Cores. Paper ARMA 87-0141 presented at the 28th U.S. Symposium on Rock Mechanics, Tucson, Arizona, USA 29 June–1 July.

Hydraulic fracturing - http://en.wikipedia.org/wiki/Hydraulic_fracturing

Itasca, 2008. Manual for PFC3D.

Junjoo P. Lee, Jon E. Olson, Jon Holder, Julia F. W. Gale and Rodrick D. Myers, 2015. The interaction of propagating opening mode fractures with preexisting discontinuities in shale. Journal of Geophysical Research. 120, 169-181.

King, George. 2012. Hydraulic fracturing 101, SPE 152596

Manchanda, Ripudamna. 2011. Mechanical, Failure and Flow Properties of Sands: Micro-Mechanical Models. Master thesis.

McKeon, M., 2011, Horizontal fracturing in shale plays.
http://www.pttc.org/workshops/eastern_062111/eastern_062111_McKeon.pdf

Mullen, M., Roundtree, R., Barree, R., and Turk, G. 2007. A Composite Determination of Mechanical Rock Properties for Stimulation Design (What to do when you do not have a sonic log). Paper SPE 108139 at the SPE Rocky Mountain Oil and Gas Technology Symposium, Denver, Co, 16-18 April.

Nolte, K.G. and Smith, M.B. 1981. Interpretation of Fracturing Pressure. JPT 33 (9): 1767–1775. SPE- 8297-PA. doi: 10.2118/8297-PA.

N. R. Warpinski, R. A. Schmidt and D. A. Northrop. "In-Situ Stresses: the Predominant Influence on Hydraulic Fracture Containment," Journal of Petroleum Technology, vol. 34, no. 3, pp. 653-664, 1982.

Olson, J, Bahorich, B, Holder, J, 2012, Examining Hydraulic Fracture-Natural Fracture Interaction in Hydrostone Block Experiments: paper presented at the SPE Hydraulic Fracturing Technology Conference, Woodlands, TX, USA, 6-8 February.

Osborn S G, Vengosh A, Warner N R and Jackson R B 2011 Methane contamination of drinking water accompanying gas-well drilling and hydraulic fracturing *Proc. Natl Acad. Sci.* 108 8172–6

Park, E.S., Martin, C. Derek, Christianson, R. 2004. Numerical simulation of the mechanical behavior of discontinuous rock masses. Proceeding of the 2nd International PFC Symposium, Kyoto, Japan, 28-29 October.

Park, Namsu. 2006. Discrete Element Modeling of Rock Fracture Behavior: Fracture Toughness and Time-dependent Fracture Growth. Ph.D. Thesis

Perkins TK, Kern LR (1961) Widths of hydraulic fractures. SPEJ 222:937–949

Potyondy, O.O. and Cundall, P.A. 2004. A bonded-particle model for rock. Int. J. Rock Mech & Geomech. 41, 1329-1364.

Renshaw, C. E. and Pollard, D. D., 1995. An experimentally verified criterion for propagation across unbounded frictional interfaces in brittle linear elastic materials. Int. J. Rock Mech & Geomech. Abs., 32 237-241.

Reynolds, S.J. and Davis, G.H., 1996. Structure Geology of Rocks and Regions: Hoboken, John Wiley & Sons, Inc., 776 p.

Safari R., Gandikota R., Mutlu U., Ji M. and Glanville J. 2013. "Pulsed Fracturing in Shale Reservoirs: Geomechanical Aspects, Ductile-Brittle Transition and Field Implications", URTEC 1579760, 12-14 August, Denver, CO.

Rickman, R., Mullen, M., Petre, E., Grieser, B., and Kundert, D., 2008 A Practical Use of Shale Petrophysics for Stimulation Design Optimization: All Shale Plays Are Not Clones of the Barnett Shale. Paper SPE 115258 presented at the 2008 SPE Annual Technical Conference and Exhibition, Denver, Colorado, U.S.A., 21-24.

Rijken, P., and M. L. Cooke, 2001, Role of shale thickness on vertical connectivity of fractures: Application of crack-bridging theory to the Austin Chalk, Texas: Tectonophysics, v. 337, p. 117– 133.

Schöpfer, M.P.J., Childs, C., Walsh, J.J., 2006. Localization of Normal Faults in Multilayer Sequences. Journal of Structural Geology 28 (2006) 816-833.

Schöpfer, M.P.J., Childs, C., Walsh, J.J.2007. Two-dimensional distinct element modelling of the structure and growth of normal faults in multilayer sequences. Part 1: model calibration, boundary conditions and selected results. Journal of Geophysical Research, 112 (2007), p. B10401

Schöpfer, M.P.J., Childs, C., Walsh, J.J.2007. Two-dimensional distinct element modelling of the structure and growth of normal faults in multilayer sequences: part 2. Impact of confining pressure and strength contrast on fault zone geometry and growth. Journal of Geophysical Research, 112 (2007), p. B10404

Shlyapobersky, J., Issa M.A., Issa, M.A., Islam, M.S., Dudley, J.W., Shulkin, Y. and Chudnovsky, A. 1998. Scale Effects on Fracture Growth Resistance in Poroelastic Media. Paper SPE 48929 presented at the Annual Technical Conference and Exhibition, New Orleans, Louisiana, USA 27–30 September. doi: 10.2118/48929-MS.

Simonson, E.R., Abou-Sayed, A.B., and Clifton, R.J. 1978. Containment of massive hydraulic fractures. SPEJ, February, 27-32. Paper SPE 6090.

Teufel, L. W. and Clark, J. A. 1984. Hydraulic Fracture Propagation in Layered Rock: Experimental Studies of Fracture Containment. SPE J. 24(1): 19-32.

Van Eekelen, H.A. 1982. Hydraulic Fracture Geometry: Fracture Containment in Layered Formations. SPE J 22 (3): 341–349. SPE- 9261-PA. doi: 10.2118/9261-PA.

Wang, W., Olson, J. E. and Prodanovic, M., 2013. Natural and Hydraulic Fracture Interaction Study Based on Semi-Circular Bending Experiments. Unconventional Resources Technology Conference (URTeC), Denver, Colorado, Aug. 12-14.

Warpinski, N.R., Fnley, S.J., Vollendorf, W.C., O'Brien, M., and Eshom, E. 1982a. The Interface Test Series: An In Situ Study of Factors Affecting the Containment of Hydraulic Fractures. Sandia National Laboratories Report No. SAND81 2408, Livermore, CA (February 1982).

Warpinski, N.R., Branagan, P.T., Peterson, R.E., and Wolhart, S.L. 1998. An Interpretation of M-Site Hydraulic Fracture Diagnostic Results. Paper SPE 39950 presented at the Rocky Mountain Regional/Low Permeability Reservoirs Symposium, Denver Colorado, USA, 5–8 April. doi: 10.2118/39950-MS.

Warpinski, N.R. and Teufel, L. W. 1987. Influence of Geologic Discontinuities on Hydraulic Fracture Propagation. J Pet Technol 39 (2): 209-220.

Wu, K 2014. Numerical Modeling of Complex Hydraulic Fracture Development in Unconventional Reservoir. Thesis

Zhang, X. and Jeffrey, R. G., 2006. The role of friction and secondary flaws on deflection and re-initiation of hydraulic fractures at orthogonal pre-existing fractures. Geophys. J. Int. 166, 1454-1465.